

EUMETSAT Satellite Application Facility on Climate Monitoring

The EUMETSAT
Network of
Satellite
Application
Facilities



CM SAF

Climate Monitoring

CM SAF Cloud, Albedo, Radiation dataset, AVHRR-based, Edition 1 (CLARA-A1)

Surface Albedo

Algorithm Theoretical Basis Document

[DOI: 10.5676/EUM_SAF_CM/CLARA_AVHRR/V001](https://doi.org/10.5676/EUM_SAF_CM/CLARA_AVHRR/V001)

Broadband Surface Albedo:

CM-60

Reference Number:


SAF/CM/FMI/ATBD/GAC/SAL

Issue/Revision Index:

1.2

Date:

11.06.2012

	EUMETSAT SAF on CLIMATE MONITORING Algorithm Theoretical Basis Document Surface Albedo CLARA-A1	Doc.No.: SAF/CM/FMI/ATBD/GAC/SAL
		Issue: 1.2
		Date: 11.06. 2012

Document Signature Table

	Name	Function	Signature	Date
Author	Aku Riihelä Terhikki Manninen Kaj Andersson	CM SAF scientists		11/06/2012
Editor	Rainer Hollmann	Science Coordinator		11/06/2012
Approval	Steering Group			26/09/2012
Release	Martin Werscheck	SAF Manager		30/11/2012



Distribution List

Internal Distribution	
Name	No. Copies
DWD Archive	1
CM SAF Team	1

External Distribution		
Company	Name	No. Copies
PUBLIC		

Document Change Record

Issue/ Revision	Date	DCN No.	Changed Pages/Paragraphs
1.0	11.06.2012	SAF/CM/FMI/ATBD/GAC/SAL	First official version presented to DRI5 review board
1.1	25.05.2012	SAF/CM/FMI/ATBD/GAC/SAL	Implementation of RID from review board
1.2	11.06.2012	SAF/CM/FMI/ATBD/GAC/SAL	Fixed bugs and implementation of last changes from DRI5 close-out - editorial update of cover page to account for DOI number and edition name - editorial update of the introduction section of CM SAF

 	<p align="center">EUMETSAT SAF on CLIMATE MONITORING</p> <p align="center">Algorithm Theoretical Basis Document Surface Albedo CLARA-A1</p>	<p>Doc.No.: SAF/CM/FMI/ATBD/GAC/SAL</p> <p>Issue: 1.2</p> <p>Date: 11.06. 2012</p>
---	---	--

Applicable documents

Reference	Title	Code
AD-1	Product user manual Surface Albedo CLARA-A1	SAF/CM/FMI/PUM/GAC/SAL/1.2
AD-2	Validation Report Surface Albedo Surface Albedo CLARA-A1	SAF/CM/FMI/VAL/GAC/SAL/1.2





 	EUMETSAT SAF on CLIMATE MONITORING Algorithm Theoretical Basis Document Surface Albedo CLARA-A1	Doc.No.: SAF/CM/FMI/ATBD/GAC/SAL Issue: 1.2 Date: 11.06. 2012
---	--	---

Table of Contents

1	THE EUMETSAT SAF ON CLIMATE MONITORING	7
2	INTRODUCTION.....	9
3	ALGORITHM OVERVIEW	10
4	ALGORITHM DESCRIPTION	12
4.1	Theoretical Description.....	12
4.1.1	Physics of the Problem	12
4.1.2	Mathematical Description of the Algorithm.....	32
4.1.3	Error Budget Estimates.....	39
4.2	SMAC atmospheric correction sensitivity study.....	40
	Assumptions and Limitations.....	50
4.2.1	Assumptions and mandatory input.....	50
4.2.2	Constraints and Limitations.....	50
	REFERENCES.....	52
	APPENDIX A. SYMBOLS AND ABBREVIATIONS	55
	APPENDIX B: SMAC NUMERIC EQUATIONS FOR CORRECTION TERMS X, Y, Z:	57

 	EUMETSAT SAF on CLIMATE MONITORING Algorithm Theoretical Basis Document Surface Albedo CLARA-A1	Doc.No.: SAF/CM/FMI/ATBD/GAC/SAL Issue: 1.2 Date: 11.06. 2012
---	--	---

List of Tables

Table 1: The average land use class albedo values derived for the USGS land use classes (http://edcdaac.usgs.gov/glcc/glcc.html) using PlaPaDa data base, urban albedo calculator and FMI radiation data of snow covered land (Breuer et al., 2003, http://ktlabo.cm.kyushu-u.ac.jp/s/pari/ALBEDO1.htm).....	22
Table 2: The rules for reclassifying USGS land cover classification to conform with available BRDF model classes.....	28
Table 3: Kernel coefficients used in CLARA-SAL BRDF correction computation. Coefficients are land cover specific. Coefficients a_{x1} are for red channel, a_{x2} are for NIR channel. (Wu et al. 1995).	36
Table 4: Estimates of error sources and their effects on the instantaneous CLARA-SAL product. All values are in relative albedo (percent).....	39

List of Figures

Figure 1: An illustration of the surface albedo product (CLARA-SAL) computation phases. The preprocessing is performed by DWD and is not a part of the actual CLARA-SAL algorithm.	10
Figure 2: Definition of the black-sky surface albedo (directional-hemispherical reflectance)	12
Figure 3: The process flow of the CLARA-SAL product.....	13
Figure 4: Location difference between apparent and true pixel locations.....	15
Figure 5: The ASTER DEM (left) and corresponding slope (middle) and azimuth (right) angle images from the Alps.	16
Figure 6: The possible sun and satellite zenith angle range for the inclined terrain case (red arrows). The flat terrain case would have a full 0 ... 90° range (blue arrows included).	17
Figure 7: The ratio of the inclined and flat terrain short wave albedo of barren land for various ground (θ_g) and sun (θ_s) inclination angle and the azimuth angle difference ($\varphi_s - \varphi_g$) values. The pink shade of the images corresponding to $\varphi_s - \varphi_g = 90^\circ$ and $\varphi_s - \varphi_g = 179^\circ$ indicates the angle combinations, which do not contribute to the reflection at all. The lines are spaced with 2 % interval. The white area shows the parameter range producing inclined terrain albedo values matching flat terrain albedo values with $\pm 1\%$ accuracy.	18
Figure 8: The ratio of the inclined and flat terrain short wave albedo of grassland for various ground (θ_g) and sun (θ_s) inclination angle and the azimuth angle difference ($\varphi_s - \varphi_g$) values. The pink shade of the images corresponding to $\varphi_s - \varphi_g = 90^\circ$ and $\varphi_s - \varphi_g = 179^\circ$ indicates the angle combinations, which do not contribute to the reflection at all. The lines are spaced with 2 % interval. The white area shows the parameter range producing inclined terrain albedo values matching flat terrain albedo values with $\pm 1\%$ accuracy.	19
Figure 9: The ratio of the inclined and flat terrain short wave albedo of cropland for various ground (θ_g) and sun (θ_s) inclination angle and the azimuth angle difference ($\varphi_s - \varphi_g$) values. The pink shade of the images corresponding to $\varphi_s - \varphi_g = 90^\circ$ and $\varphi_s - \varphi_g = 179^\circ$ indicates the angle combinations, which do not contribute to the reflection at all. The lines are spaced with 2 % interval. The white area shows the parameter range producing inclined terrain albedo values matching flat terrain albedo values with $\pm 1\%$ accuracy.	20
Figure 10: The ratio of the inclined and flat terrain short wave albedo of forested land for various ground (θ_g) and sun (θ_s) inclination angle and the azimuth angle difference ($\varphi_s - \varphi_g$) values. The pink shade of the images corresponding to $\varphi_s - \varphi_g = 90^\circ$ and $\varphi_s - \varphi_g = 179^\circ$ indicates the angle combinations, which do not contribute to the reflection at all. The lines are spaced with 2 % interval. The white area shows the parameter range producing inclined terrain albedo values matching flat terrain albedo values with $\pm 1\%$ accuracy.	21
Figure 11: The histogram of the true terrain and flat terrain albedo ratio values for the Alpine test area for two sun and satellite angle cases. Left) The sun zenith angle was 31 °, the sun azimuth angle was 141°, the satellite zenith angle was 25° and the satellite azimuth angle was 181°. Right) The sun zenith angle was 70 °, the sun azimuth angle was 118°, the satellite zenith angle was 50° and the satellite azimuth angle was 181°.....	23



 	EUMETSAT SAF on CLIMATE MONITORING Algorithm Theoretical Basis Document Surface Albedo CLARA-A1	Doc.No.: SAF/CM/FMI/ATBD/GAC/SAL Issue: 1.2 Date: 11.06. 2012
---	--	---

Figure 12: The difference between the flat terrain and true terrain albedo values at the Alps. The slope and aspect values were derived from ASTER DEMs and the land use classes from USGS land use map. The sun zenith angle was 31 °, the sun azimuth angle was 141°, the satellite zenith angle was 25° and the satellite azimuth angle was 181° 24

Figure 13: The difference between the flat terrain and true terrain albedo values at the Alps. The slope and aspect values were derived from ASTER DEMs and the land use classes from USGS land use map. The sun zenith angle was 70 °, the sun azimuth angle was 118°, the satellite zenith angle was 50° and the satellite azimuth angle was 181° 25

Figure 14: The difference between the flat terrain and true terrain albedo values at the Alps. A detail of Figure 12 (left) and Figure 13 (right) has been median filtered to 1 km resolution to correspond to the CLARA-SAL product. The colour code is the same as in those two Figures. 26

Figure 15: The BRDF geometry and relevant angles. For all non-isotropic objects, the reflectance changes as the illumination (subscript s) and viewing (subscript v) angles for elevation and azimuth change. 28

Figure 16: Satellite zenith and azimuth angles of successful CLARA-SAL retrievals during 2008 at DYE-2 in Greenland (66.48N, -46.28E). The polar plots show viewing (satellite) zenith angles in the radial axis and viewing azimuth angles in the angular axis. 31

Figure 17: SMAC correction effect (above) and relative retrieval error caused by an assumption of AOD=0.1 (below) for grassland at VIS channel with Rtoa=0.12 (left) and at NIR channel with Rtoa=0.35 (right). SZA=VZA=45 degrees. 41

Figure 18: MISR average AOD at 555nm between January-December 2010 42

Figure 19: SMAC correction effect (above) and relative retrieval error caused by an assumption of AOD=0.1 (below) for grassland at VIS channel with Rtoa=0.12 (left) and at NIR channel with Rtoa=0.35 (right). SZA=VZA=55 degrees. 43

Figure 20: The impact of using a constant AOD on the resulting broadband albedo in Case 2. Above: the calculated broadband albedo using various AOD values in the atmospheric correction. Below: Relative error in the broadband albedo calculated using AOD=0.1 relative to using a 'true' AOD value. 44



Figure 21: SMAC correction effect (above) and relative retrieval error caused by an assumption of AOD=0.1 (below) for a desert target at VIS channel with Rtoa=0.32 (left) and at NIR channel with Rtoa=0.35 (right). SZA=35, VZA=45 degrees. RAZI=40 deg. Blue curves show the correction effect if desert SMAC coefficients are used instead of continental ones. 45

Figure 22: SMAC correction as a function of AOD and Relative Azimuth Angle. Correction magnitude shown for a desert target (Rtoa=0.32) with continental coefficients as in SAL computation. O3 concentration constant at 0.35, SZA=55, VZA=50 degrees. 46

Figure 23: SMAC correction effect (above) and relative retrieval error caused by an assumption of O3=0.35 [atm cm] (below) for grassland at VIS channel with Rtoa=0.12 (left) and at NIR channel with Rtoa=0.35 (right). SZA=VZA=45 degrees, AOD kept constant at 0.1. 47

Figure 24: The impact of using a constant O3 on the resulting broadband albedo in Case 4. Above: the calculated broadband albedo using various O3 values in the atmospheric correction. Below: Relative error in the broadband albedo calculated using O3=0.35[atm cm] relative to using a 'true' AOD value. 48

Figure 25: An example of the contribution of terms in Liang NTBC equation to the total broadband albedo. Inputs of Case 1 used (vegetated grassland, average viewing geometry). 49

 	EUMETSAT SAF on CLIMATE MONITORING Algorithm Theoretical Basis Document Surface Albedo CLARA-A1	Doc.No.: SAF/CM/FMI/ATBD/GAC/SAL Issue: 1.2 Date: 11.06. 2012
---	--	---

1 The EUMETSAT SAF on Climate Monitoring

The importance of climate monitoring with satellites was recognized in 2000 by EUMETSAT Member States when they amended the EUMETSAT Convention to affirm that the EUMETSAT mandate is also to “contribute to the operational monitoring of the climate and the detection of global climatic changes”. Following this, EUMETSAT established within its Satellite Application Facility (SAF) network a dedicated centre, the SAF on Climate Monitoring (CM SAF, <http://www.cmsaf.eu>).



The consortium of CM SAF currently comprises the Deutscher Wetterdienst (DWD) as host institute, and the partners from the Royal Meteorological Institute of Belgium (RMIB), the Finnish Meteorological Institute (FMI), the Royal Meteorological Institute of the Netherlands (KNMI), the Swedish Meteorological and Hydrological Institute (SMHI), the Meteorological Service of Switzerland (MeteoSwiss), and the Meteorological Service of the United Kingdom (UK MetOffice). Since the beginning in 1999, the EUMETSAT Satellite Application Facility on Climate Monitoring (CM SAF) has developed and will continue to develop capabilities for a sustained generation and provision of Climate Data Records (CDR's) derived from operational meteorological satellites.

In particular the generation of long-term data sets is pursued. The ultimate aim is to make the resulting data sets suitable for the analysis of climate variability and potentially the detection of climate trends. CM SAF works in close collaboration with the EUMETSAT Central Facility and liaises with other satellite operators to advance the availability, quality and usability of Fundamental Climate Data Records (FCDRs) as defined by the Global Climate Observing System (GCOS). As a major task the CM-SAF utilizes FCDRs to produce records of Essential Climate Variables (ECVs) as defined by GCOS. Thematically, the focus of CM SAF is on ECVs associated with the global energy and water cycle.



Another essential task of CM SAF is to produce data sets that can serve applications related to the new Global Framework of Climate Services initiated by the WMO World Climate Conference-3 in 2009. CM SAF is supporting climate services at national meteorological and hydrological services (NMHSs) with long-term data records but also with data sets produced close to real time that can be used to prepare monthly/annual updates of the state of the climate. Both types of products together allow for a consistent description of mean values, anomalies, variability and potential trends for the chosen ECVs. CM SAF ECV data sets also serve the improvement of climate models both at global and regional scale.

As an essential partner in the related international frameworks, in particular WMO SCOPE-CM (Sustained COordinated Processing of Environmental satellite data for Climate Monitoring), the CM SAF - together with the EUMETSAT Central Facility, assumes the role as main implementer of EUMETSAT's commitments in support to global climate monitoring. This is achieved through:

- Application of highest standards and guidelines as lined out by GCOS for the satellite data processing,
- Processing of satellite data within a true international collaboration benefiting from developments at international level and pollinating the partnership with own ideas and standards,
- Intensive validation and improvement of the CM SAF climate data records,
- Taking a major role in data set assessments performed by research organisations such as WCRP. This role provides the CM SAF with deep contacts to research organizations that form a substantial user group for the CM SAF CDRs,
- Maintaining and providing an operational and sustained infrastructure that can serve the community within the transition of mature CDR products from the research community into operational environments.

 	<p align="center">EUMETSAT SAF on CLIMATE MONITORING</p> <p align="center">Algorithm Theoretical Basis Document Surface Albedo CLARA-A1</p>	<p>Doc.No.: SAF/CM/FMI/ATBD/GAC/SAL</p> <p>Issue: 1.2</p> <p>Date: 11.06. 2012</p>
---	---	--

A catalogue of all available CM SAF products is accessible via the CM SAF webpage, www.cmsaf.eu/. Here, detailed information about product ordering, add-on tools, sample programs and documentation is provided.

 	<p align="center">EUMETSAT SAF on CLIMATE MONITORING</p> <p align="center">Algorithm Theoretical Basis Document Surface Albedo CLARA-A1</p>	<p>Doc.No.: SAF/CM/FMI/ATBD/GAC/SAL</p> <p>Issue: 1.2</p> <p>Date: 11.06. 2012</p>
---	--	--



2 Introduction

Surface albedo is one of the factors governing the Earth's radiation budget, which in turn drives the climate of our planet. Surface albedo is the dimensionless ratio of hemispherical reflected radiation to the hemispherical incoming radiation. It has been designated as one of the Essential Climate Variables (ECV) of the GCOS, as required by IPCC and UNFCCC (GCOS Secretariat 2006) . Because of surface albedo's significance to the radiation budget, its continuous monitoring is of considerable importance in understanding climate variability and change.

Many climatological applications require knowledge of surface albedo values and trends, and thus it needs to be observed on a broad scale both temporally and spatially. Ground-based observations rarely satisfy both requirements due to practicality issues. Airborne observations are better, but still expensive over the timescales required by climate studies, i.e. 25 years or more. Satellite remote sensing is currently the most cost-effective observation method that provides data on a global scale, with reasonable accuracy and revisit periods. Satellite instruments such as AVHRR have matured into legacy instruments, i.e., the length of their data series will reach climate scales in the foreseeable future.

The objective of this document is to offer the reader with a detailed look into how the Global Area Coverage Surface Albedo (CLARA-SAL) Long-term Dataset of EUMETSAT's CM SAF is created. A general outlook of the product(s) and the data format details are available in the CLARA-SAL product user manual (AD-1). The accuracy of the product(s) is described in the validation report (AD-2).

All the major algorithms are based on peer-reviewed publications. The product was originally overseen by Dr. Vesa Laine of FMI, with the programming overseen by Dr. Kaj Andersson of VTT. The development and validation of this version of CLARA-SAL is overseen by Dr. Terhikki Manninen and Mr. Aku Riihelä of FMI. The product is computed operationally by the CM SAF operations team at the European Center for Medium-range Weather Forecasts (ECMWF).

 	EUMETSAT SAF on CLIMATE MONITORING Algorithm Theoretical Basis Document Surface Albedo CLARA-A1	Doc.No.: SAF/CM/FMI/ATBD/GAC/SAL Issue: 1.2 Date: 11.06. 2012
---	--	---

3 Algorithm Overview

This document describes the process of deriving surface broadband albedo from satellite observation for the 1st Edition of the GACSAL long-term dataset.

The process of deriving a broadband surface albedo product from satellite radiance observations is challenging. The radiation of the Sun must first propagate the Earth's atmosphere, then be scattered from the Earth's surface, and propagate the atmosphere again going up before it is observed by the satellite instruments. All of these factors influence the observed radiation and thereby they must be compensated for in the algorithm to ensure a non-biased retrieval of the surface albedo. All of these will be discussed in detail in later chapters, but for now the reader is encouraged to see Figure 1 for a general outline of the albedo computation stages.

The Surface Albedo (CLARA-SAL) TCDR of the Satellite Application Facility on Climate Monitoring (CM SAF) is produced as a part of the EUMETSAT distributed ground segment. The product is derived from the AVHRR instrument aboard the NOAA satellites.

The definition of broadband albedo for this product is the wavelength range of 0.25 - 2.5 μm , according to the narrow-to-broadband (NTBC) algorithms that ultimately determine the range. The full solar spectrum extends further into infrared, but it should be kept in mind that the regions of 2.5 - 4 μm contribute as little as 0.03% to the total broadband albedo (van Leeuwen, W.J.D. and Roujean, J.L. 2002). AVHRR channels 1 and 2 (0.58-0.68 μm and 0.725-1 μm) are used for the CLARA-SAL product generation as radiance sources.

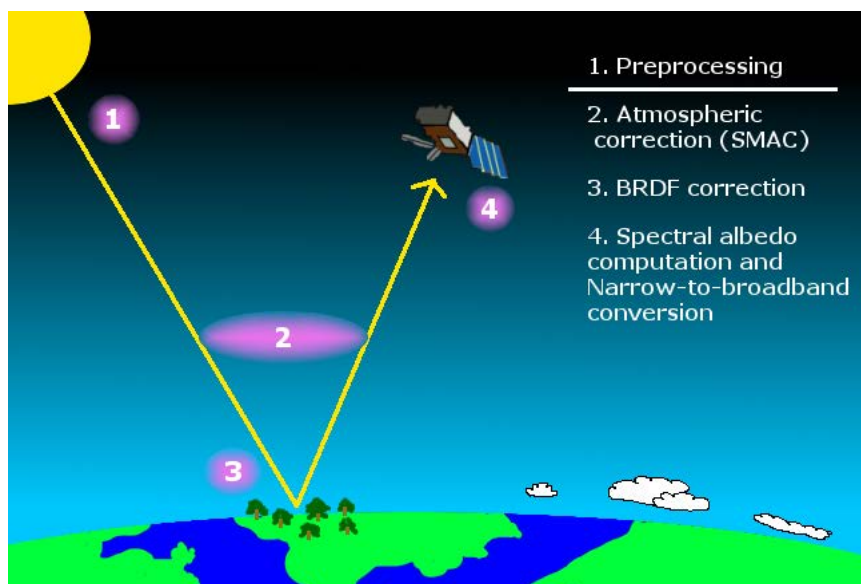




Figure 1: An illustration of the surface albedo product (CLARA-SAL) computation phases. The preprocessing is performed by DWD and is not a part of the actual CLARA-SAL algorithm.


The CLARA-SAL data record spans the Earth completely from pole to pole. The spatial resolution of the CLARA-SAL product is 0.25 degrees, although instantaneous product

 	EUMETSAT SAF on CLIMATE MONITORING Algorithm Theoretical Basis Document Surface Albedo CLARA-A1	Doc.No.: SAF/CM/FMI/ATBD/GAC/SAL Issue: 1.2 Date: 11.06. 2012
---	--	---

processing occurs at nominal GAC resolution (~5 km at nadir). Products provided to users are the pentad and monthly means of instantaneous AVHRR-GAC broadband albedo images.

On process flow terms, the algorithm set up as shown in Fig. 2. Details concerning user messaging, error detection and other details have been omitted for clarity. The main processing steps in deriving the broadband surface albedo product from observed satellite radiances are as follows:

1. The radiances are converted into pixelwise Top-of-atmosphere (TOA) reflectances. This preprocessing step is accomplished via external processing modules based on PPS software package. More information is available in section 4.1.1.1.
2. A radiometric and geolocation topography correction is performed. The correction implementation is described in section 4.1.1.2.
3. The TOA reflectances are reduced to surface reflectances by removing the atmospheric effects with a correction based on the SMAC algorithm (Rahman and Dedieu 1994). See section 4.1.1.3 for details.
4. The surface reflectances are expanded into hemispherical spectral albedos by applying a BRDF algorithm based on the work of Roujean et al. (1992) and Wu et al. (1995). The BRDF algorithm is applied to both 0.6 and 0.8 μm channel separately. For pixels classified as being covered by snow, the correction for BRDF effects is handled at the weekly and monthly level by a temporal averaging of the various directional reflectances derived as the instantaneous product. Thus, over- or underestimations of the mean pentad/monthly snow albedo will occur in the instantaneous CLARA-SAL images.
5. The spectral albedos are processed to a shortwave broadband albedo via a narrow-to-broadband (NTB) conversion. The conversion is both instrument and pixel land cover specific. The land cover information comes from USGS land use classification data. The NTBC algorithm is chosen as follows:
 - For water pixels, the BB albedo is taken from a LUT after Jin et al. (2004).
 - For snow pixels, the instantaneous BB directional reflectance is computed from the spectral directional reflectance (see above) by an NTBC algorithm by Xiong et al. (2002).
 - For other types of land cover, the NTBC conversion takes place based on an algorithm by Liang (2000).
6. Sun Zenith Angle normalization was not included in this first Edition for technical reasons and to preserve coherency between land and snow albedo retrievals. Its effect is considered a part of the retrieval uncertainty of the pentad/monthly mean products.

	<p style="text-align: center;">EUMETSAT SAF on CLIMATE MONITORING</p> <p style="text-align: center;">Algorithm Theoretical Basis Document Surface Albedo CLARA-A1</p>	<p>Doc.No.: SAF/CM/FMI/ATBD/GAC/SAL</p> <p>Issue: 1.2</p> <p>Date: 11.06. 2012</p>
---	--	--

4 Algorithm Description

4.1 Theoretical Description

The description of the CLARA-SAL algorithm is divided into two parts. First, the subsection titled Physics of the Problem will go over the various parts of the computation, describing them in a qualitative manner and providing details on the physical requirements on the algorithm. The next subsection, Mathematical Description of the Algorithm, will provide a concise representation of the actual mathematical formulae applied. Figures 1 and 2 provide illustrative details on the computation process.

4.1.1 Physics of the Problem

The physical quantity that CLARA-SAL describes is the black-sky broadband surface albedo, mathematically written as (Schaepman-Strub et al., 2006)

$$\alpha(\theta_s, \phi_s) = \int_0^{2\pi} \int_0^{\pi/2} \rho(\theta_s, \phi_s; \theta_v, \phi_v) \cos(\theta_v) \sin(\theta_v) d\theta_v d\phi_v \quad (1)$$

The black-sky surface albedo is the integral of radiation reflected from a single incident direction (θ_s, ϕ_s) towards all viewing directions (θ_v, ϕ_v) in the zenithal and azimuthal planes, as described by the reflectance ρ . The angles are illustrated in Figure 2. The spectral dependency of albedo is omitted here; a full broadband albedo would be obtained by integrating the directional-hemispherical reflectance (black-sky albedo) over the waveband under investigation. CLARA-SAL is a broadband albedo product, defined with a wavelength range of 0.25 - 2.5 μm .

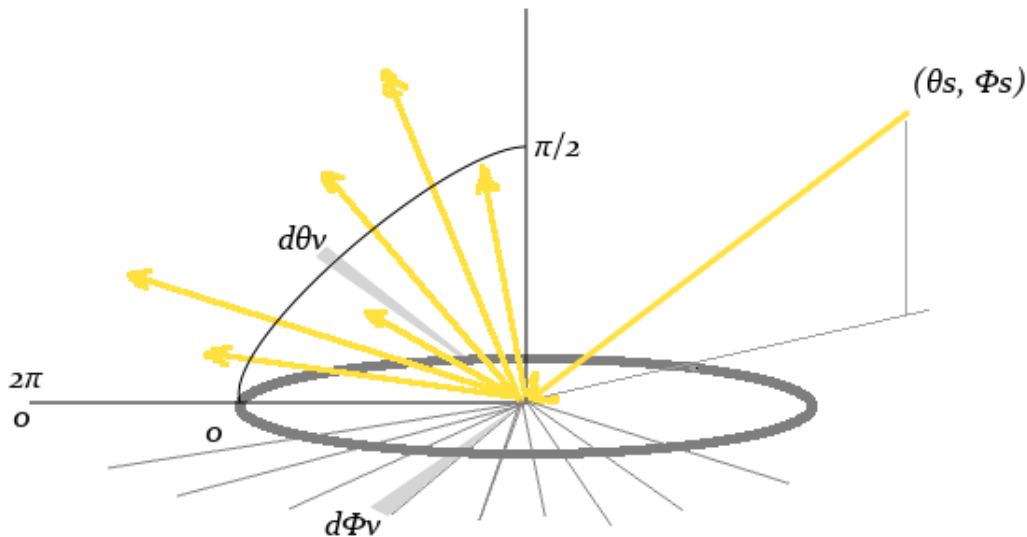



Figure 2: Definition of the black-sky surface albedo (directional-hemispherical reflectance)

The derivation of the directional-hemispherical (black-sky) broadband surface albedo from monodirectional radiances observed by a satellite in an orbit of 870 (NOAA) kilometers is a challenging physical problem. The radiance observed by the satellite instrument represents

	<p align="center">EUMETSAT SAF on CLIMATE MONITORING</p> <p align="center">Algorithm Theoretical Basis Document</p> <p align="center">Surface Albedo CLARA-A1</p>	<p>Doc.No.: SAF/CM/FMI/ATBD/GAC/SAL</p> <p>Issue: 1.2</p> <p>Date: 11.06. 2012</p>
---	--	--

only a single viewing and illumination geometry (*BRDF problem*), the observed radiances are limited in wavelength by the instruments' spectral response (*spectral conversion problem*), and the radiances contain a contribution from the scattering mechanisms of the atmosphere between the instrument and the observed surface (*atmospheric problem*). The wavelength ranges of the radiation emission from the atmosphere can be neglected because the instrument channels used to derive the surface albedo are beyond the thermal emission wavelengths. In addition, many pixels are partly or completely contaminated by cloud cover. The reflectance properties of most clouds also resemble snow quite closely. Both of these issues must be solved to exempt the cloud-contaminated pixels from the computation and to identify cloud-free snow and sea ice pixels for later computation (*Cloud mask problem*).

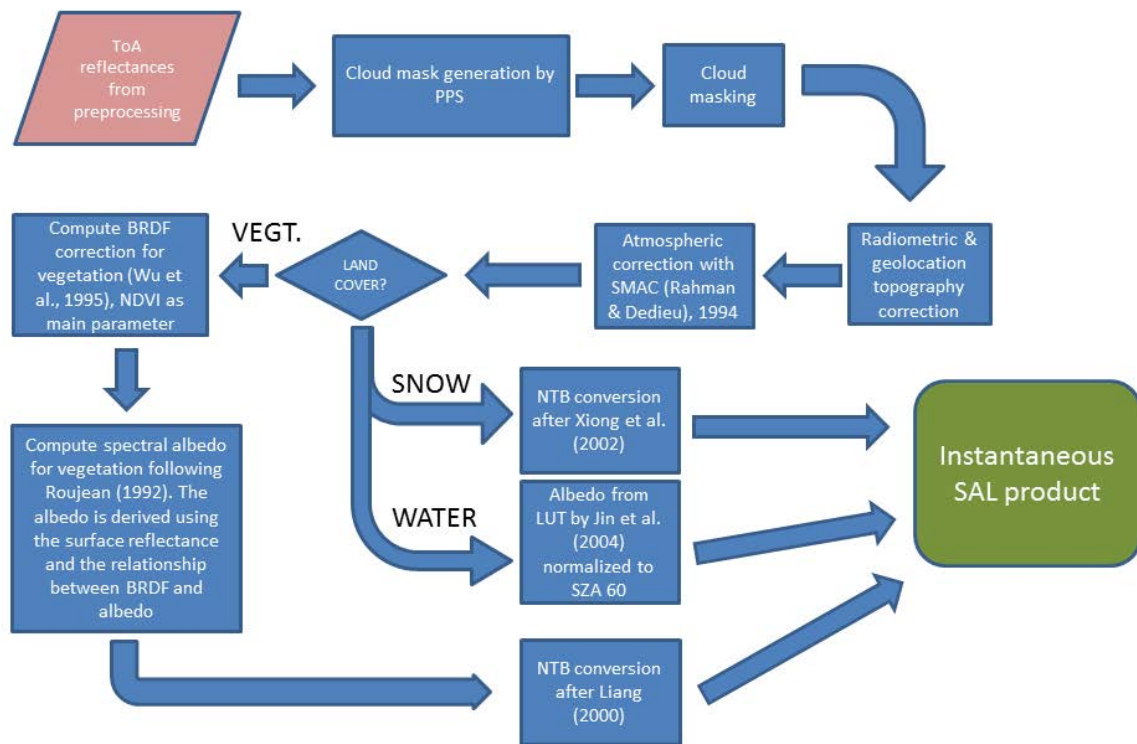




Figure 3: The process flow of the CLARA-SAL product.

 	EUMETSAT SAF on CLIMATE MONITORING Algorithm Theoretical Basis Document Surface Albedo CLARA-A1	Doc.No.: SAF/CM/FMI/ATBD/GAC/SAL Issue: 1.2 Date: 11.06. 2012
---	--	---

4.1.1.1 Processing of TOA reflectances and Cloud mask

The TOA reflectances used as CLARA-SAL input are derived by the PPS software package from the AVHRR instrument counts using the algorithm by Heidinger et al. (2010). The process creates the Fundamental Climate Data Record (FCDR) of AVHRR normalized radiances with respect to irradiance at the top of atmosphere. The Heidinger algorithm recalibrates AVHRR radiances using simultaneous MODIS overpasses at nadir viewing geometry during the MODIS data period (2000-2009). For the older AVHRR period, targets with stable surface reflectance (Libyan Desert and Dome-C on Antarctica) were characterized by MODIS observations and then assumed to be fully stable calibration points for the rest of the AVHRR data series.

Sun-Earth distance variation is also accounted for in the preprocessing. A separate preprocessing script for CLARA-SAL then corrects for the Sun Zenith angle difference from 0 degrees (the so-called cosine correction).

The identification of cloudy pixels in the AVHRR images is performed by the PPS software package in the pre-processing stage. Its detailed performance description is beyond the scope of this document. Details on the AVHRR-PPS package and cloud mask derivation may be found in Dybbroe et al. (2005). Basically, the input cloud mask for CLARA-SAL uses sophisticated thresholding algorithms to classify each observed pixel into one of four categories: clear, cloud contaminated, cloud filled, and snow. Of these, only clear and snow pixels proceed to further computation of CLARA-SAL.

The cloud mask is retrieved by the PPS software and provided to CLARA-SAL as input data. The cloud mask is retrieved at nominal GAC resolution, thus it is directly applicable data for CLARA-SAL processing. Partially cloudy pixels are assumed to be correctly classified by the cloud mask.


Cloud shadows are not specifically handled, as it is assumed that the coarse GAC resolution (~5km) compensates for shadowing issues. It is possible that this assumption fails at low Sun elevation conditions, but the processing is always limited to Sun Zenith Angles below 70 degrees. Therefore we found no need for a cloud shadow correction at this time.

The flawless functioning of the cloud mask product is essential for the accuracy of CLARA-SAL. The cloud mask is particularly challenged by snow and cloud delineation, unfavourable illumination conditions, and cloud detection over coast lines. The effects of classification errors will be discussed in more detail in section 4.1.3.

4.1.1.2 Topography correction

The topography affects the satellite image in first order in two ways: 1) the altitude difference with respect to sea level will cause the geolocation of the pixel to be shifted and 2) the inclination of the slopes of the terrain within a pixel will alter its reflectance value. As the BRDF calculations are based on a horizontal plane assumption, erroneous values will be obtained for inclined slopes. In addition, the slope distribution of the terrain covered by the pixel may contain slopes that are not seen at all by the sun or the satellite. These kinds of situations will cause even larger errors than small slope inclinations.

The calculation of topography effects requires that full illumination-viewing geometry data is available. To accommodate this need, the PPS preprocessing package now provides CLARA-SAL with all relevant angular data: satellite zenith angles, Sun zenith angles, satellite azimuth angles, and Sun azimuth angles. If only the relative azimuth angle data (difference

	<p align="center">EUMETSAT SAF on CLIMATE MONITORING</p> <p align="center">Algorithm Theoretical Basis Document</p> <p align="center">Surface Albedo CLARA-A1</p>	<p>Doc.No.: SAF/CM/FMI/ATBD/GAC/SAL</p> <p>Issue: 1.2</p> <p>Date: 11.06. 2012</p>
---	--	--

between Sun and satellite azimuths) is available, CLARA-SAL attempts to calculate the Sun azimuth using swath location data and timestamp. Satellite azimuth is then calculated based on the Sun and relative azimuth data. However, this calculation is approximative and should be considered as a back-up solution for cases in which the full angular dataset is not available for some reason. The calculation is adapted from the solar geometry algorithms in the 6S radiative transfer code (Vermeete et al., 1997).

Multiple reflections from slope to slope would be a second order effect affecting the observable reflectance. However, the first order correction already involves CPU-intensive calculations so the second order effect is not studied here at all.

The PPS software provides latitude/longitude co-ordinates for each image pixel. These co-ordinates have been computed from satellite attitude data without any information of the terrain altitude, and are thus not accurate for elevated areas at higher view angles. A true elevation of 3000 meters causes a pixel shift of 2500 m when the viewing angle is 40 degrees. Thus the effect can be significant.

The following figure shows how the DEM is used for computing the true pixel location from the apparent one. Initial pixel co-ordinates refer to locations on the geoid surface. Computing true locations shift pixels closer to the nadir on elevated areas, but some pixels may be left in shade. Pixel dimensions also change on tilted areas.

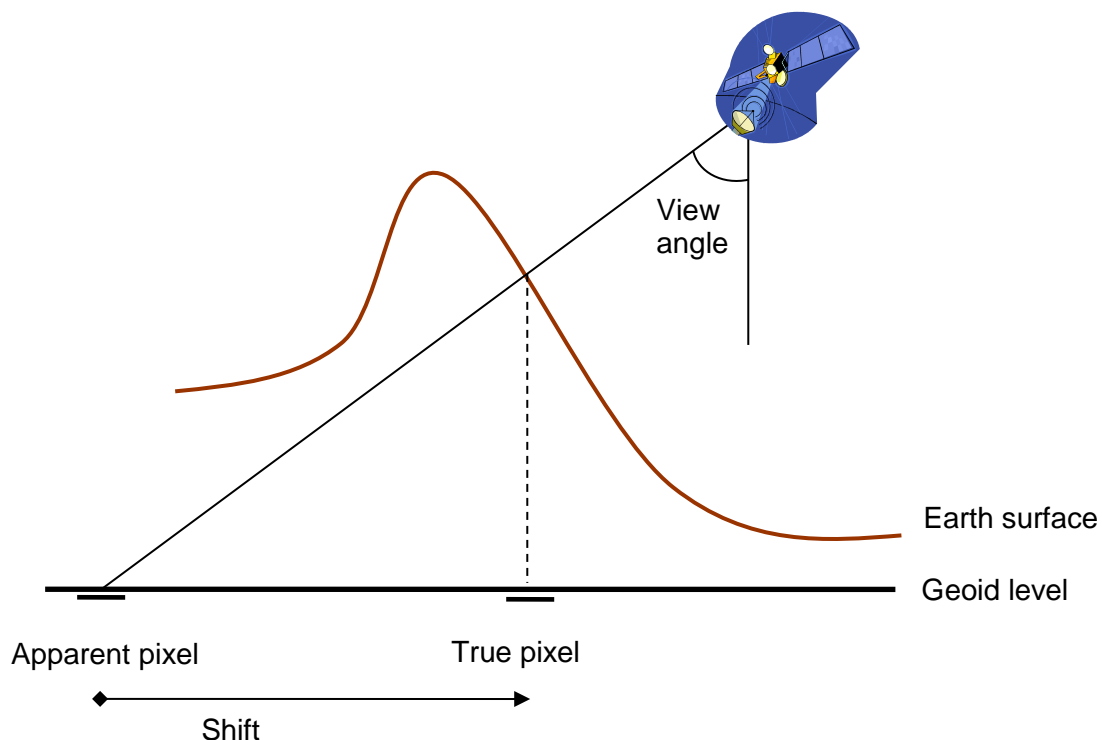




Figure 4: Location difference between apparent and true pixel locations.

The BRDF function used in the albedo calculations has been derived for flat terrain (Roujean et al. 1992). Therefore it is essential to study theoretically the errors that the flat terrain assumption may cause in mountainous areas. For this purpose a few ASTER DEMs with

 	EUMETSAT SAF on CLIMATE MONITORING Algorithm Theoretical Basis Document Surface Albedo CLARA-A1	Doc.No.: SAF/CM/FMI/ATBD/GAC/SAL Issue: 1.2 Date: 11.06. 2012
---	--	---

30 m x 30 m pixel size were acquired from the Alps (Figure 5). The maximum height in that area is 4208 m and the maximum slope is 88°. All aspect angle values naturally exist there, but peaks in the angle distribution are at about 135°, 316° and 226°. Thus the area is not isotropic from the point of view of the sun or a satellite.

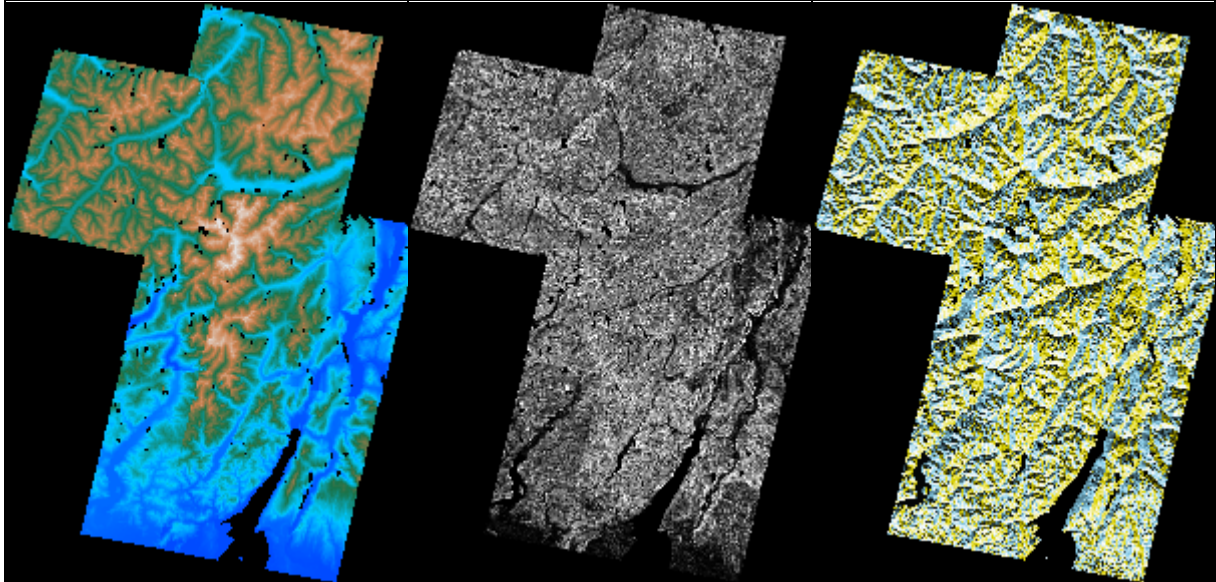


Figure 5: The ASTER DEM (left) and corresponding slope (middle) and azimuth (right) angle images from the Alps.

For albedo calculation the BRDF function is needed to describe the 3D-complexity of the target. In the existing version of the CLARA-SAL product all pixels are assumed to be horizontal and the BRDF function used is directly that derived for flat terrain (Roujean et al. 1992). If topography information were available the BRDF function of horizontal flat terrain could take the inclination into account just replacing the global angles by the corresponding local angles, i.e. angles with respect to the normal of the terrain pixel. Like for horizontal flat terrain one has to take into account that the pixel should receive sunlight, for which the condition is

$$\sin(\theta_s)\sin(\theta_g)\cos(\varphi_s - \varphi_g) + \cos(\theta_s)\cos(\theta_g) \geq 0 \quad (2)$$

Moreover, the satellite should also see the pixel, so that

$$\sin(\theta_v)\sin(\theta_g)\cos(\varphi_v - \varphi_g) + \cos(\theta_v)\cos(\theta_g) \geq 0 \quad (3)$$

where the notation used is

θ_s = Global sun zenith angle

θ_v = Global satellite zenith angle


θ_g = DEM slope angle

θ_s' = Local sun zenith angle

θ_v' = Local satellite zenith angle

φ_s = Global sun azimuth angle

φ_v = Global satellite azimuth angle

	EUMETSAT SAF on CLIMATE MONITORING Algorithm Theoretical Basis Document Surface Albedo CLARA-A1	Doc.No.: SAF/CM/FMI/ATBD/GAC/SAL Issue: 1.2 Date: 11.06. 2012
---	--	---

φ_g = DEM azimuth angle

φ_s' = Local sun azimuth angle

φ_v' = Local satellite azimuth angle

The relationships between the local and global sun and satellite angles are

$$\begin{aligned} \cos(\theta_s') &= \sin(\theta_s)\sin(\theta_g)\cos(\varphi_s - \varphi_g) + \cos(\theta_s)\cos(\theta_g) \\ \cos(\theta_v') &= \sin(\theta_v)\sin(\theta_g)\cos(\varphi_v - \varphi_g) + \cos(\theta_v)\cos(\theta_g) \end{aligned} \quad (4)$$

The difference between the horizontal terrain and inclined terrain case is, that no light comes from below the horizon and the satellite can't see the terrain from below the horizon (Figure 6). Thus the only difference in calculating the BRDF function for inclined terrain is that the variation range of θ_s' and θ_v' is less than $0 \dots \pi/2$. The effect of the inclination and azimuth angles of the pixel on the shortwave albedo is estimated for various land cover types in Figure 7 to Figure 10

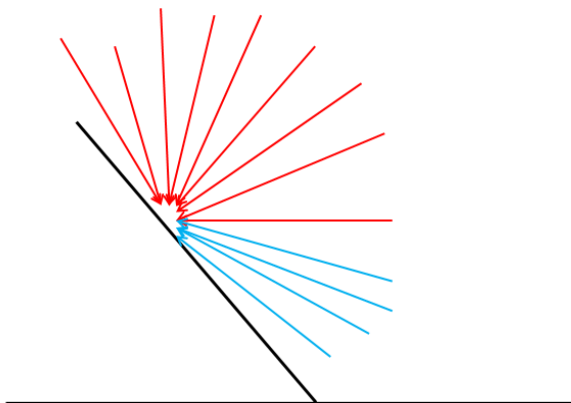


Figure 6: The possible sun and satellite zenith angle range for the inclined terrain case (red arrows). The flat terrain case would have a full $0 \dots 90^\circ$ range (blue arrows included).

Basically all the land use types have the same kind of errors. When the azimuth angle difference between the terrain normal and the sun viewing direction is larger than 90° , the inclined terrain values would be larger than those of flat terrain, unless the pixel is not seen by the sun or the satellite, when the albedo value is then zero.

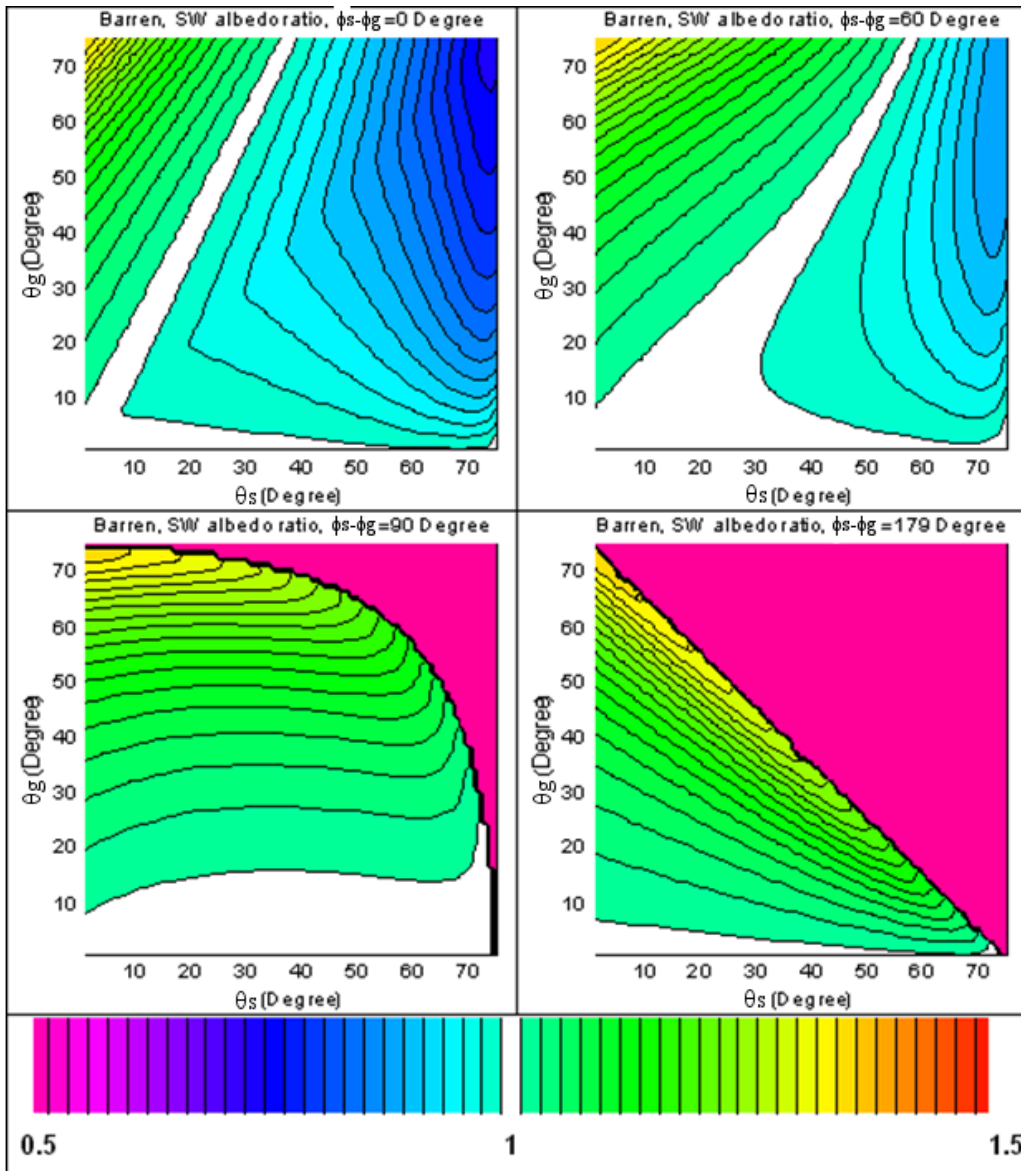


Figure 7: The ratio of the inclined and flat terrain short wave albedo of barren land for various ground (θ_g) and sun (θ_s) inclination angle and the azimuth angle difference ($\phi_s - \phi_g$) values. The pink shade of the images corresponding to $\phi_s - \phi_g = 90^\circ$ and $\phi_s - \phi_g = 179^\circ$ indicates the angle combinations, which do not contribute to the reflection at all. The lines are spaced with 2 % interval. The white area shows the parameter range producing inclined terrain albedo values matching flat terrain albedo values with $\pm 1\%$ accuracy.

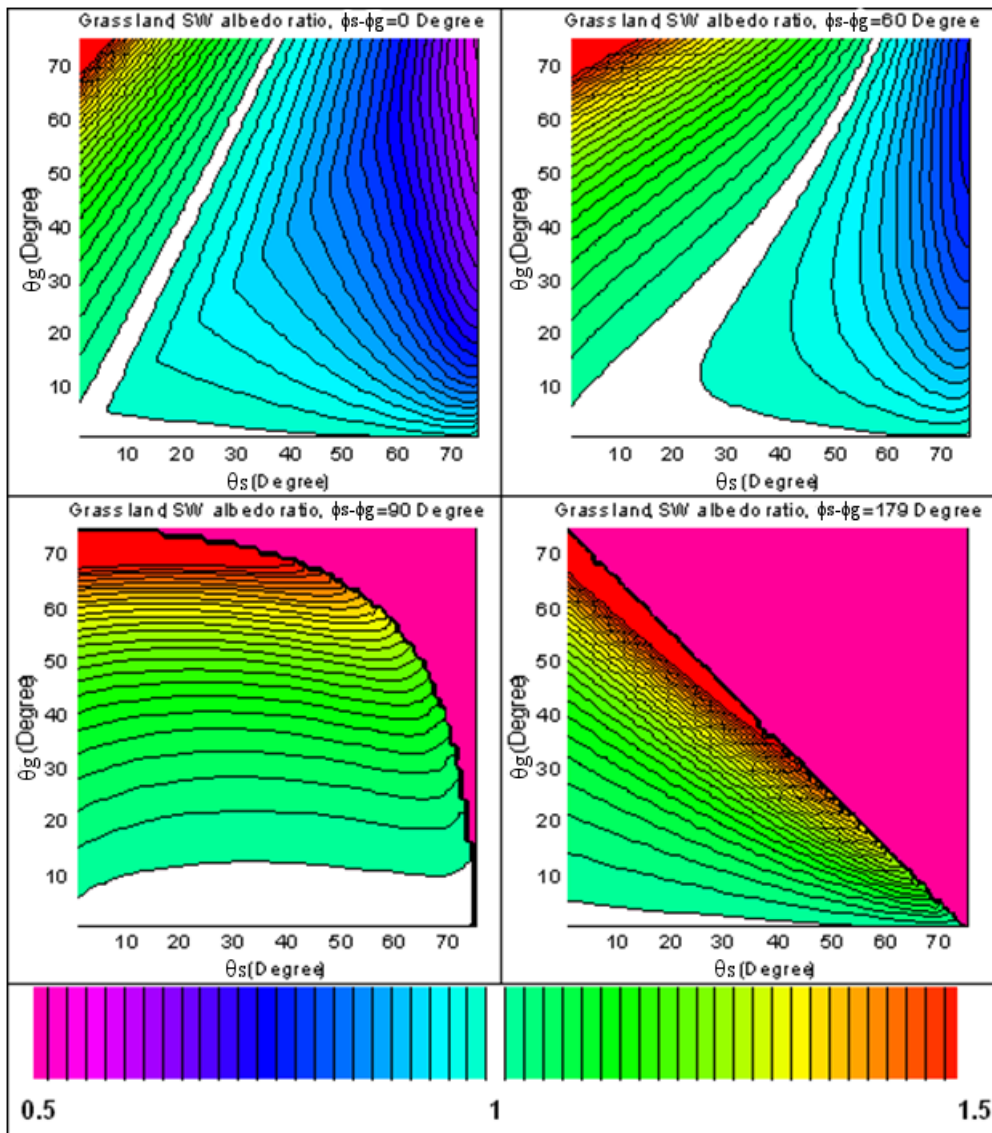


Figure 8: The ratio of the inclined and flat terrain short wave albedo of grassland for various ground (θ_g) and sun (θ_s) inclination angle and the azimuth angle difference ($\varphi_s - \varphi_g$) values. The pink shade of the images corresponding to $\varphi_s - \varphi_g = 90^\circ$ and $\varphi_s - \varphi_g = 179^\circ$ indicates the angle combinations, which do not contribute to the reflection at all. The lines are spaced with 2 % interval. The white area shows the parameter range producing inclined terrain albedo values matching flat terrain albedo values with $\pm 1\%$ accuracy.

If the sun zenith angle is large (>60 degrees) and the azimuthal difference between the ground normal and the sun viewing direction is moderate (<70 degrees), the inclined terrain albedo values would be smaller than the flat terrain albedo values. For smaller sun elevation ($0 \dots 40$ degrees, depending on the ground inclination angle) and moderate azimuthal difference the inclined terrain would have higher albedo values than the flat terrain. When the azimuth angle difference increases the probability of the inclined terrain albedo to go to zero increases and when the azimuth angle difference is larger than 180° , the albedo value of inclined terrain will be zero independently of the slope steepness and the sun zenith angle. Although increasing slope angle naturally increases the difference between the inclined and

flat terrain albedo value, the azimuth angle of the slope has a larger effect due to complete shadowing probability being so high (larger than 50 % for uniform azimuth angle distribution).

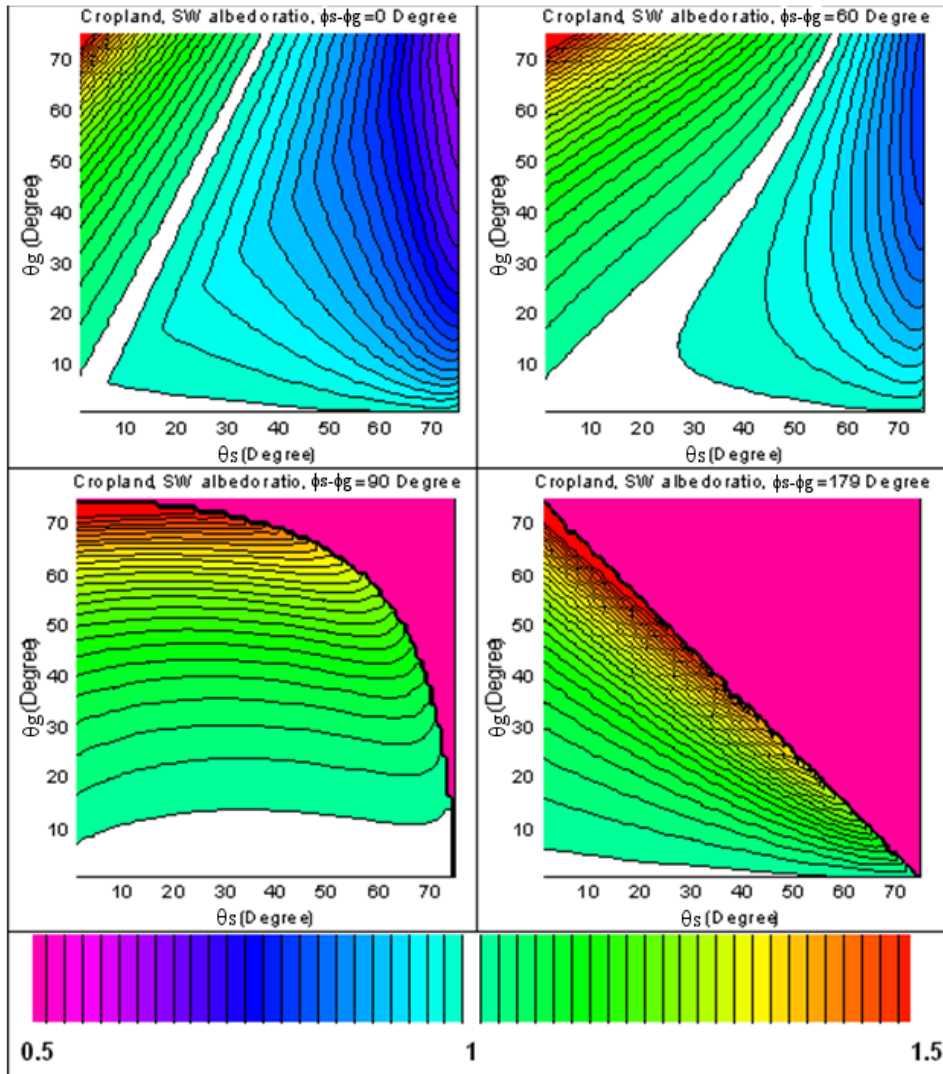


Figure 9: The ratio of the inclined and flat terrain short wave albedo of cropland for various ground (θ_g) and sun (θ_s) inclination angle and the azimuth angle difference ($\varphi_s - \varphi_g$) values. The pink shade of the images corresponding to $\varphi_s - \varphi_g = 90^\circ$ and $\varphi_s - \varphi_g = 179^\circ$ indicates the angle combinations, which do not contribute to the reflection at all. The lines are spaced with 2 % interval. The white area shows the parameter range producing inclined terrain albedo values matching flat terrain albedo values with $\pm 1\%$ accuracy.

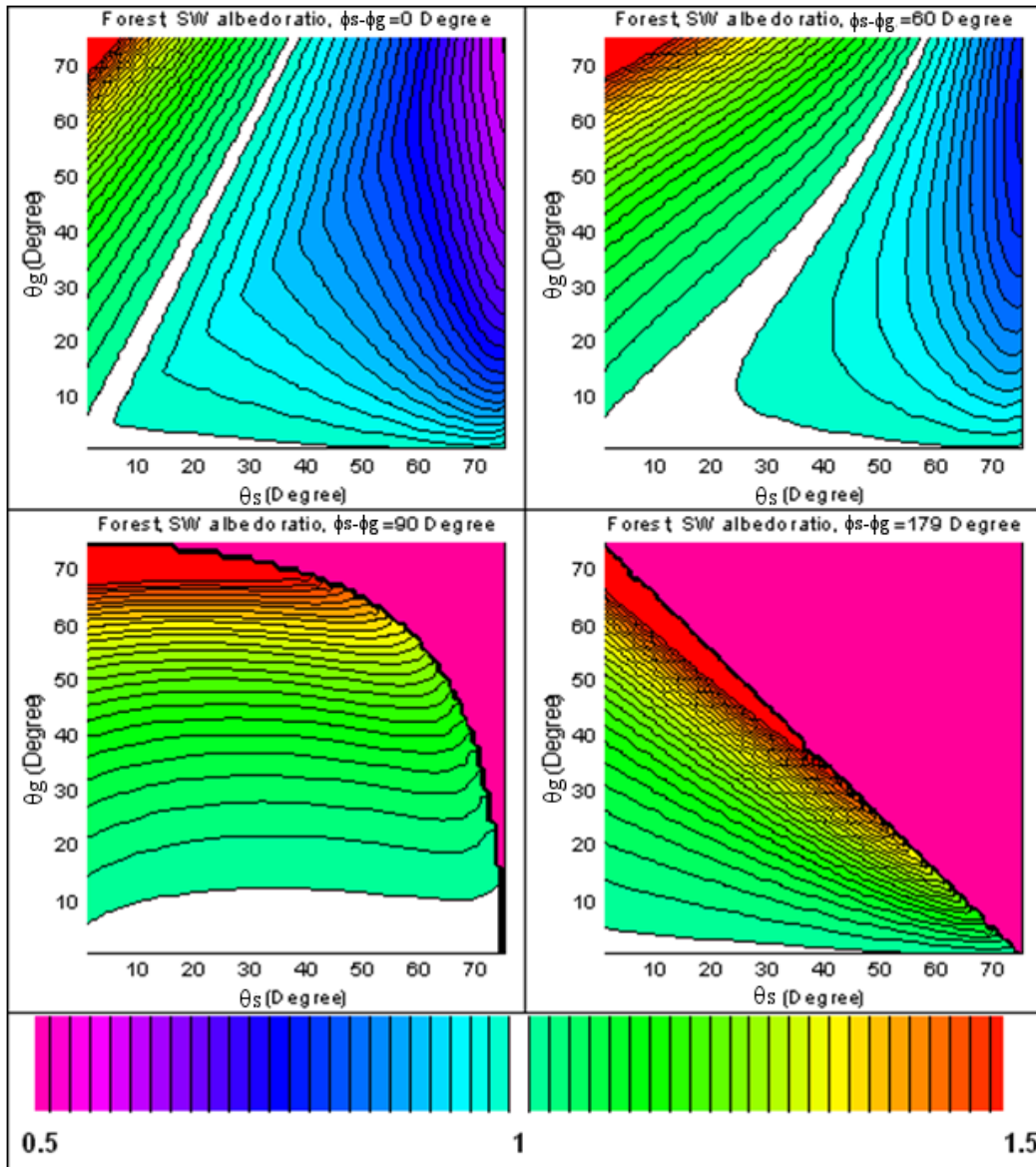




Figure 10: The ratio of the inclined and flat terrain short wave albedo of forested land for various ground (θ_g) and sun (θ_s) inclination angle and the azimuth angle difference ($\varphi_s - \varphi_g$) values. The pink shade of the images corresponding to $\varphi_s - \varphi_g = 90^\circ$ and $\varphi_s - \varphi_g = 179^\circ$ indicates the angle combinations, which do not contribute to the reflection at all. The lines are spaced with 2 % interval. The white area shows the parameter range producing inclined terrain albedo values matching flat terrain albedo values with $\pm 1\%$ accuracy.

The effect of the topography on the albedo of the Alpine test area was calculated using the ASTER slope and aspect images and the USGS land use class map. The histograms of the ratio of the true and flat terrain albedos are shown for two sun and satellite angle cases in Figure 11. The first case is a favourable one the sun and satellite having as high elevation as realistic and the latter case is an unfavourable one the sun and satellite having their acceptable lower limit zenith angle values. In both cases both overestimates and underestimates of the albedo value will appear, but when the sun and satellite elevation are small (< 20 degrees), the inclined terrain tends to have even smaller values.

 	EUMETSAT SAF on CLIMATE MONITORING Algorithm Theoretical Basis Document Surface Albedo CLARA-A1	Doc.No.: SAF/CM/FMI/ATBD/GAC/SAL Issue: 1.2 Date: 11.06. 2012
---	--	---

Since the albedo values vary also with the land use classes the net effect of the topography can be estimated only by calculating the absolute albedo values. The albedo difference images have been produced according to

$$\Delta \text{ albedo} = \text{ class albedo} * (1 - \text{ albedoratio}) \quad (5)$$

where the *albedo ratio* is the ratio of the true terrain and flat terrain albedos and the *class albedo* is taken from Table 1.

Table 1: The average land use class albedo values derived for the USGS land use classes (<http://edcdaac.usgs.gov/glcc/glcc.html>) using PlaPaDa data base, urban albedo calculator and FMI radiation data of snow covered land (Breuer et al., 2003, <http://ktlabo.cm.kyushu-u.ac.jp/s/pari/ALBEDO1.htm>).

	USGS Land use class	Average albedo in percent
1	100 Urban and Built-Up Land	33
2	211 Dryland Cropland and Pasture	23
3	212 Irrigated Cropland and Pasture	23
4	213 Mixed Dryland/Irrigated Cropland and Pasture	23
5	280 Cropland/Grassland Mosaic	23
6	290 Cropland/Woodland Mosaic	23
7	311 Grassland	32
8	321 Shrubland	32
9	330 Mixed Shrubland/Grassland	32
10	332 Savanna	32
11	411 Deciduous Broadleaf Forest	18
12	412 Deciduous Needleleaf Forest	18
13	421 Evergreen Broadleaf Forest	18
14	422 Evergreen Needleleaf Forest	18
15	430 Mixed Forest	18
16	500 Water Bodies	5
17	620 Herbaceous Wetland	32
18	610 Wooded Wetland	18
19	770 Barren or Sparsely Vegetated	23
20	820 Herbaceous Tundra	32
21	810 Wooded Tundra	32
22	850 Mixed Tundra	32
23	830 Bare Ground Tundra	23
24	900 Snow or Ice	70

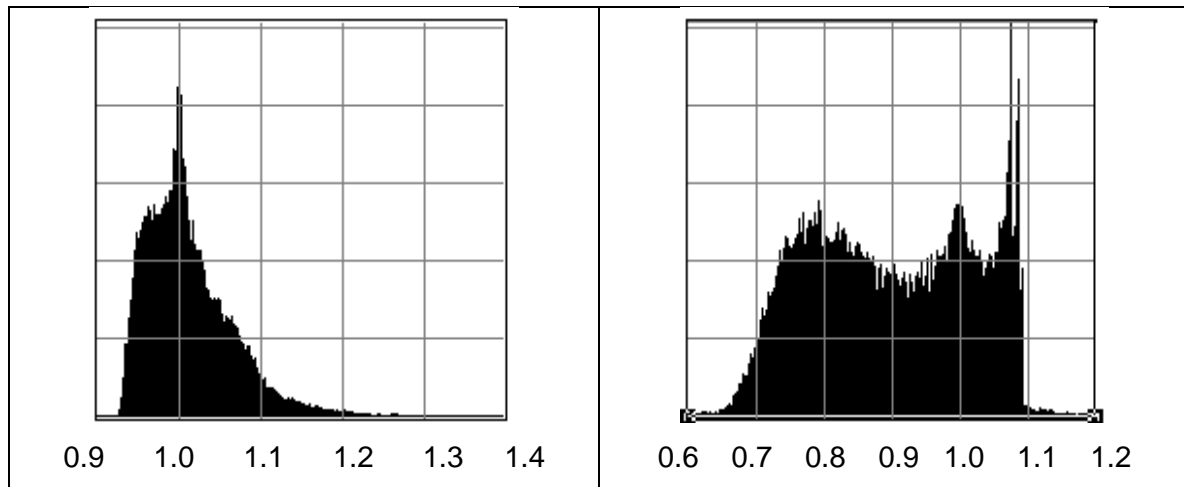


Figure 11: The histogram of the true terrain and flat terrain albedo ratio values for the Alpine test area for two sun and satellite angle cases. Left) The sun zenith angle was 31 °, the sun azimuth angle was 141°, the satellite zenith angle was 25° and the satellite azimuth angle was 181°. Right) The sun zenith angle was 70 °, the sun azimuth angle was 118°, the satellite zenith angle was 50° and the satellite azimuth angle was 181°.

The difference between the flat terrain albedo and the true terrain albedo is shown in Figure 12 and Figure 13 for the two sun and satellite constellations. Typically the albedo of slopes is overestimated. This is natural, since completely shaded slopes have zero albedo values in the image. The mountain tops are covered with permanent snow and there the flat terrain albedo value tends to be smaller than that of inclined terrain. The underestimated land use pixels clearly identifiable in Figure 12 belong to the urban land use class for which the same BRDF function type is used as for barren areas. Possibly the average value of urban class of Table 1 is too high representing more just the city centre albedo, so that the albedo difference is then too large.

In order to estimate the effect of the topography on AVHRR, details of Figure 12 and Figure 13 have been median filtered to 1 km x 1 km resolution (Figure 14). Averaging would have caused too drastic effects, because of some extreme values of the albedo ratio. Although the flat terrain albedo values are reasonably good for the favourable sun and satellite constellation, the composite albedo products contain also images corresponding to the unfavourable case, especially at high latitudes where the sun elevation is never high. Thus it is obvious that in rough topography the slope and aspect angles should be taken into account in estimating the BRDF function. Mostly this concerns mountainous areas, but also terrain of moderate height variation may have a quite distinct slope structure.

For the needs of BRDF function the 1 km resolution slope and aspect data sets available in the internet (<http://edcdaac.usgs.gov/1KM/1kmhomepage.html>) are not suitable. On the other hand ASTER DEMs are nowadays available only in limited areas. However, new higher resolution global DEMs are gradually being distributed by the internet (for example, <ftp://edcftp.cr.usgs.gov/pub/data/srtm/>). The addition of topography information to the surface albedo processing is an issue of further investigation.

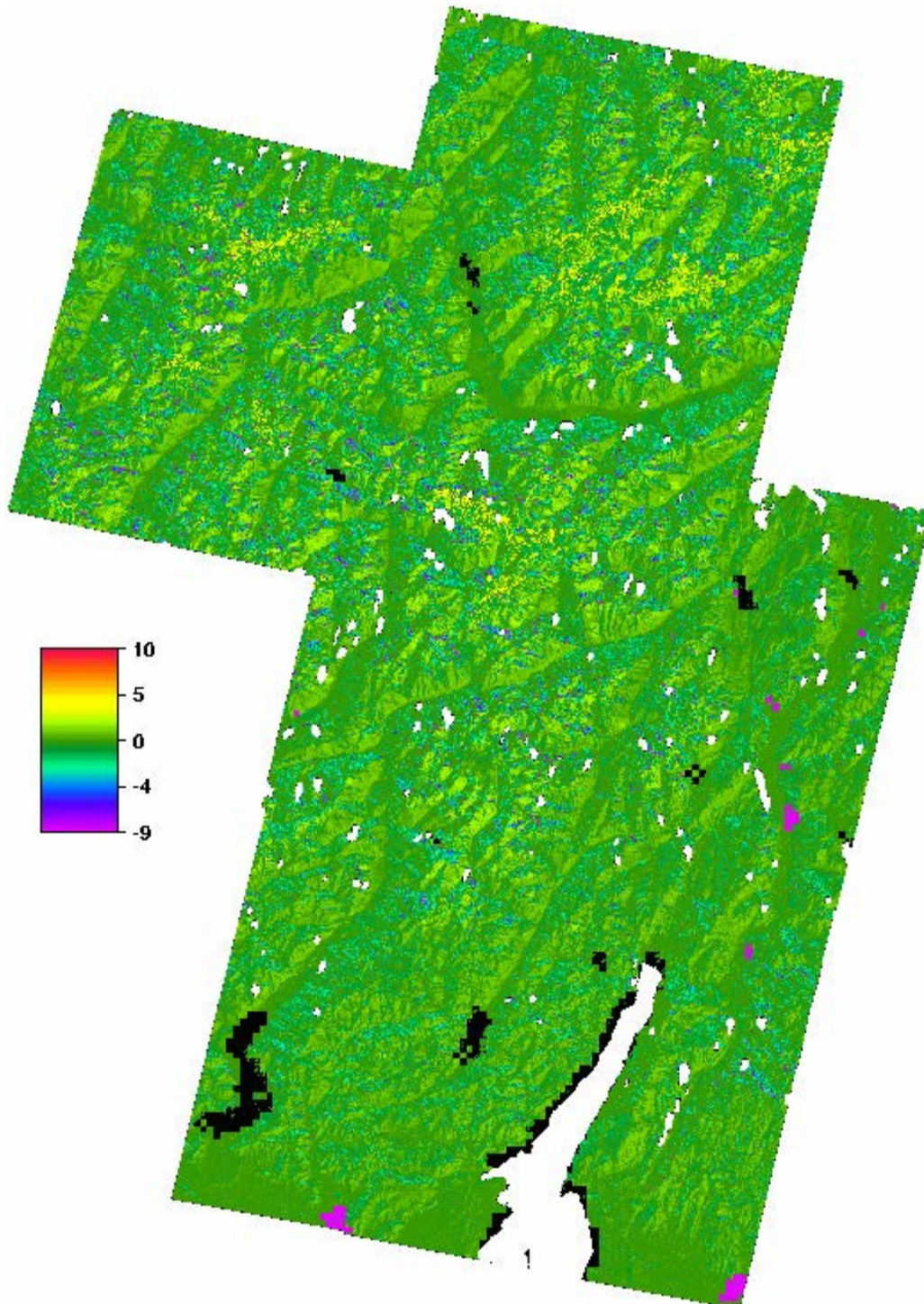


Figure 12: The difference between the flat terrain and true terrain albedo values at the Alps. The slope and aspect values were derived from ASTER DEMs and the land use classes from USGS land use map. The sun zenith angle was 31 °, the sun azimuth angle was 141°, the satellite zenith angle was 25° and the satellite azimuth angle was 181°

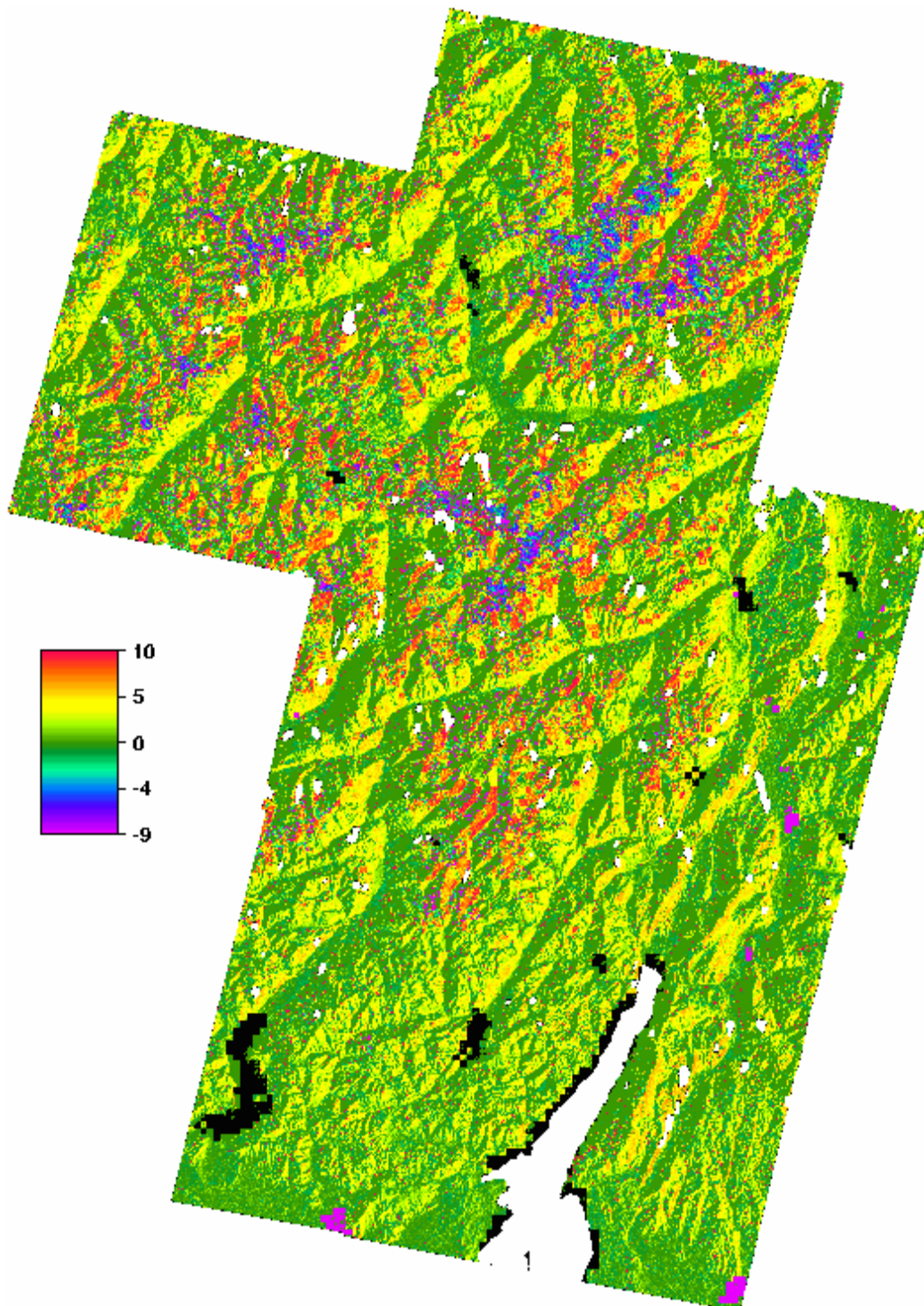




Figure 13: The difference between the flat terrain and true terrain albedo values at the Alps. The slope and aspect values were derived from ASTER DEMs and the land use classes from USGS land use map. The sun zenith angle was 70 °, the sun azimuth angle was 118°, the satellite zenith angle was 50° and the satellite azimuth angle was 181°.

 	EUMETSAT SAF on CLIMATE MONITORING Algorithm Theoretical Basis Document Surface Albedo CLARA-A1	Doc.No.: SAF/CM/FMI/ATBD/GAC/SAL Issue: 1.2 Date: 11.06. 2012
---	--	---

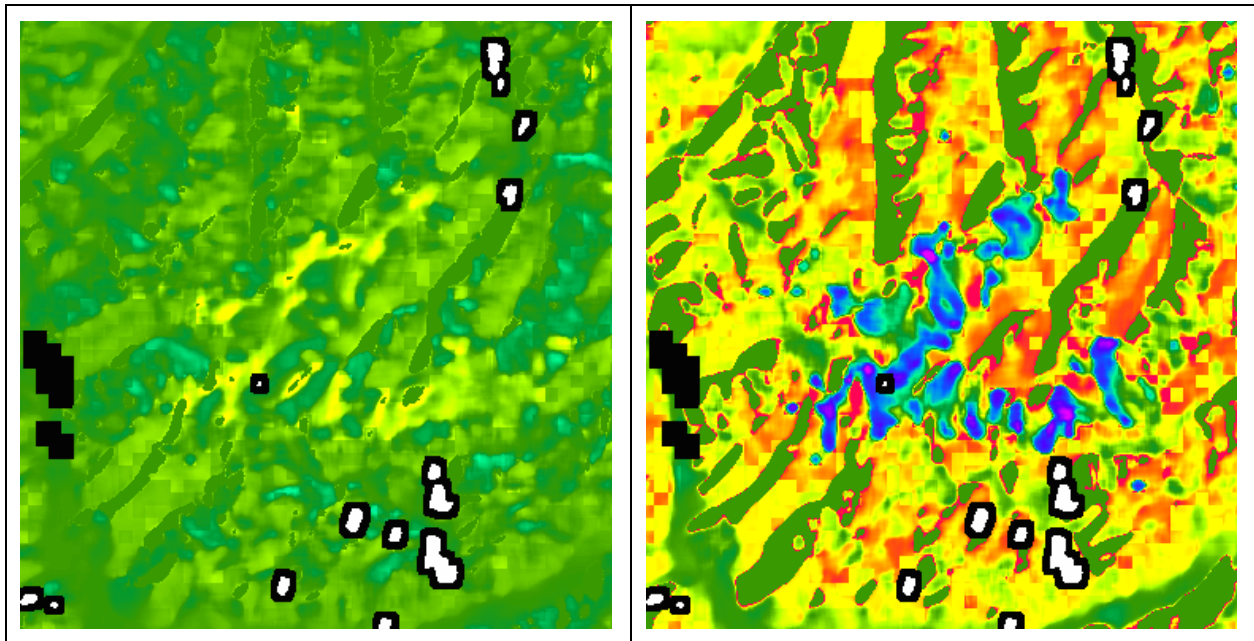




Figure 14: The difference between the flat terrain and true terrain albedo values at the Alps. A detail of Figure 12 (left) and Figure 13 (right) has been median filtered to 1 km resolution to correspond to the CLARA-SAL product. The colour code is the same as in those two Figures.

Although the topography correction related to the slopes of the terrain can be determined, when the albedos of the individual slope areas are known, the inverse problem can not be solved deterministically. The reason is that slopes not seen by the sun or the satellite have not contributed to the reflectance value at all, but the topographically corrected surface albedo value of a pixel should be the average of all individual slope area albedo values, when the slopes areas would be in horizontal position. For the shaded pixels the individual albedo values are missing. For an individual image it is not always realistic to assume that the shaded slopes would have the average value of the existing slopes. However, the end products are pentad and monthly averages, which consist of varying illumination and viewing directions, so that the slopes visible and shaded will be different in the various images. Therefore it is assumed that taking the average albedo value of visible slopes is a reasonable estimate for the shaded slopes.

The calculation of the BRDF for the inclined slopes just assuming that the local incidence and viewing angles have to be used instead of global is a good assumption for many land cover classes, such as snow and sand. For forests one should basically take into account that the tree trunks are often essentially vertical even when the ground is tilted. However, the BRDF model used for forests (Roujean et al. 1992) treats the canopy as a layer of random scatterers without any special attention to tree trunks. Yet the grouping of the trees will affect the radiation characteristics of a canopy. Probably this effect will just average out in coarse resolution images. Hence it is considered justified to use the BRDF model also for forests on inclined slopes.

4.1.1.3 Atmospheric scattering

The atmospheric effect is in a way an external artefact in the input from the surface albedo viewpoint, so it must be removed first. The algorithm chosen to perform this is the Simplified

 	EUMETSAT SAF on CLIMATE MONITORING Algorithm Theoretical Basis Document Surface Albedo CLARA-A1	Doc.No.: SAF/CM/FMI/ATBD/GAC/SAL Issue: 1.2 Date: 11.06. 2012
---	--	---

Method for Atmospheric Corrections (SMAC) (Rahman and Dedieu 1994). The algorithm uses the following input for each pixel:

- TOA reflectance, from PPS pre-processing output
- Surface pressure, from ECMWF ERA-Interim data [hPa]
- Ozone content, uses a constant of 0.35 [$\frac{atm}{cm^2}$] for this Edition
- Aerosol optical depth at 550 nm, uses a constant of 0.1 for this Edition
- Total column water vapour content, from ECMWF ERA-Interim data [$\frac{g}{cm^2}$]

The algorithm is based on the 6S radiative transfer model code, but is simplified to greatly enhance computation speed. The main simplification is the treatment of the various atmospheric radiative components (e.g. Rayleigh scattering) by analytic terms, which are sensor- and waveband-specific. The data volumes processed to derive the distributable CM SAF CLARA-SAL products are large, and therefore speed is essential. The requirement for SMAC usage is that the averaged atmospheric coefficients must be determined in advance by a best fit against the full 6S radiative transfer model. Ozone content and aerosol optical depth are kept constant for the time being due to processing resource limitations. Spatially and temporally resolved AOD input will be included in the future if a robust AOD dataset for the coverage period is found.

The algorithm also provides the option of computing the correction separately for desert areas, because the atmosphere behaves differently in extremely dry conditions with high aerosol content. However, because the currently used land use classification information (USGS) does not contain the desert class, this option is not used and all SMAC corrections are computed with continental correction coefficients. The effect of this may be noticeable over deserts, and will be elaborated upon in chapter 0.

4.1.1.4 BRDF

Once the observed radiances have been calibrated into TOA reflectances, interfering clouds have been removed and the atmospheric effects removed, the product is an image of bidirectional surface reflectances. At this point the product represents only the viewing and illumination geometry at the moment of imaging. To expand the surface reflectance into spectral (hemispherical) albedo, a method is needed to describe the behavior of the reflectance with different viewing and illumination geometries. This is often referred to as an *anisotropy correction*. If the surface reflected equally to all directions, this correction would not be necessary. However, all natural surfaces have some degree of anisotropy.

To account for the anisotropy, a mathematical relation capable of explaining the reflectance dependence on viewing and illumination angles is needed. This relation is called the Bidirectional Reflectance Distribution Function (BRDF), and its modeling and use have been widely discussed in literature. The term was first introduced by Nicodemus (1970) , who defined the angular dependence of reflectance (i.e. BRDF) mathematically as

$$\rho(\theta_s, \varphi_s; \theta_v, \varphi_v) = \frac{dL_v(\theta_v, \varphi_v)}{dE_s(\theta_s, \varphi_s)} \quad (6)$$

where dL_v is the (differential) radiance reflected by the object in the direction specified by the zenithal reflection angle (θ_v) and azimuthal reflection angle (φ_v). dE_s is the (differential) irradiance received by the object from the radiation source in the direction specified by its zenithal incidence angle (θ_s) and azimuthal incidence angle (φ_s). The geometries are further illustrated in Figure 15.

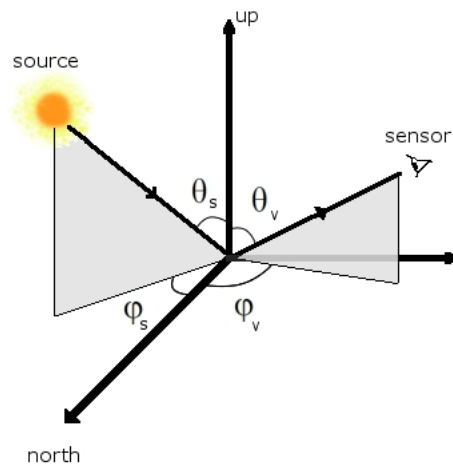


Figure 15: The BRDF geometry and relevant angles. For all non-isotropic objects, the reflectance changes as the illumination (subscript s) and viewing (subscript v) angles for elevation and azimuth change.

There are a large number of different BRDF models in existence. The most popular ones for remote sensing applications are the so-called kernel models, named after the fact that they model the reflectance of any surface type as a combination of isotropical, volume and geometrical scattering contributions (or kernels). In general terms the kernel reflectance models can be described as in Roujean et al. (1992) and Wu et al. (1995) by:

$$\rho = k_0 + k_1 f_1(\theta_s, \theta_v, \varphi) + k_2 f_2(\theta_s, \theta_v, \varphi) \quad (7)$$


where the angles are as defined above, subscript 0 denotes nadir reflectance, subscript 1 denotes geometrical scattering term, and subscript 2 denotes volume scattering term. The model is valid for the waveband over which its kernels are defined. The k terms are the geometric and volume scattering kernels, and the f terms are their associated viewing and illumination angle dependency functions.

The BRDF needs to be calculable entirely from satellite observations and *a priori* known auxiliary data to be useful for the computation of CLARA-SAL. The BRDF model chosen for this task is the one by Wu et al. (1995). It uses NDVI as the parameter describing vegetation canopy physiology (through the K coefficients), and three angular parameters $\theta_s, \theta_v, \varphi$ as shown in eq. 7. It is based on the BRDF model by Roujean et al. (1992), and therefore works with a geometric approach to scattering modeling. The original model was modified with fits to AVHRR data to allow the usage of NDVI and to account for seasonal phenologically induced BRDF variation. The model coefficients were derived separately for specific land cover types. Therefore the model may be called semiempirical.

The BRDF coefficients are separate for forest, barren, grassland, cropland and snow land cover types (coefficient values are listed in section 3.1.2). But modern LUC datasets contain a larger set of classes than that. To use the BRDF model, the LUC dataset is checked for conformance to USGS classification types and compressed as given in Table 2.

Table 2: The rules for reclassifying USGS land cover classification to conform with available BRDF model classes

USGS class	BRDF class
------------	------------

	EUMETSAT SAF on CLIMATE MONITORING Algorithm Theoretical Basis Document Surface Albedo CLARA-A1	Doc.No.: SAF/CM/FMI/ATBD/GAC/SAL
		Issue: 1.2 Date: 11.06. 2012

1, 19, 23	Barren
11, 12, 13, 14, 15	Forest
2, 3, 4, 5, 6	Cropland
7, 8, 9, 10, 17, 18, 20, 21, 22	Grassland
24	Snow
16	Water

It should be noted that the BRDF correction may have some inaccuracies in areas where the recorded land use classification does not correspond well to the physical characteristics of the scene. An example of this might be a tilled field where no green vegetation exists. CLARA-SAL attempts to remove some such effects by classifying the pixel as "Barren" if its NDVI value is below 0.1, regardless of its USGS type. Also, man-made LUC changes may cause erroneous BRDF corrections because the LUC data is not updated regularly. The effects of both errors will be discussed in section 4.1.3.

The MODIS BRDF kernels could be considered as an alternative to the current NDVI-based kernels. However, they are temporally incompatible with the CLARA-SAL processing needs. The MODIS BRDF are distributed as a 16-day mean. As the CLARA-SAL product is based on instantaneous satellite images, the use of temporally averaged BRDF kernels would lead to incorrect results during periods of marked phenological changes or snow melt.

Wu's equations give the anisotropy factor Ω from eq.7 (the BRDF relative to the nadir reflectance)

$$\Omega_i(\theta_s, \theta_v, \varphi) = \frac{\rho_i(\theta_s, \theta_v, \varphi)}{k_0} = 1 + a_{1i}f_1(\theta_s, \theta_v, \varphi) + a_{2i}f_2(\theta_s, \theta_v, \varphi) \quad (8)$$

The first term on the right is 1 because the nadir reflectance $\rho_i(0,0,\varphi) = k_0$ (Wu et al. 1995). Therefore the other coefficients are $a_{1i} = k_1/k_0$ and $a_{2i} = k_2/k_0$. The subindex i is either 1 or 2, representing the AVHRR channels 1 or 2 for which this model was developed for.

In the CLARA-SAL algorithm, the anisotropy factor is first used to normalize the surface reflectance to a common viewing and illumination geometry of zenith Sun, nadir view using (Li 1996)

$$\rho(0,0,\varphi) = \frac{\Omega(0,0,\varphi)}{\Omega(\theta_s,\theta_v,\varphi)} * \rho_{surf}(\theta_s, \theta_v, \varphi) \quad (9)$$

Knowledge of the BRDF can also be used to derive the spectral albedo directly from surface reflectances through integration over all viewing directions. This relation is used in CLARA-SAL to derive the spectral albedo with the integrated formula and angular terms by Roujean et al. (1992), combined with kernel coefficients by Wu et al. (1995)



$$\alpha(\theta_s) = \rho(0,0,\varphi) * (1 + a_{1i}I_1 + a_{2i}I_2) \quad (10)$$

keeping in mind that $\alpha(\theta_s) = k_0 + k_1I_1 + k_2I_2$, $a_i = k_i/k_0$ and $\rho(0,0,\varphi) = k_0$ (Roujean et al., 1992 and Wu et al, 1995).

The integrated forms of the angular dependency terms are

$$I_1 = -0.9946 - 0.0281\tan \theta_s - 0.0916\tan^2 \theta_s + 0.0108\tan^3 \theta_s \quad (11)$$

$$I_2 = -0.0137 + 0.0370\tan \theta_s + 0.0310\tan^2 \theta_s - 0.0059\tan^3 \theta_s \quad (12)$$

 	EUMETSAT SAF on CLIMATE MONITORING Algorithm Theoretical Basis Document Surface Albedo CLARA-A1	Doc.No.: SAF/CM/FMI/ATBD/GAC/SAL Issue: 1.2 Date: 11.06. 2012
---	--	---

The algorithm result $\alpha(\theta_s)$ at this stage is a spectral albedo for red and NIR wavelengths. The albedo corresponds to the sun zenith angle at the time of satellite observation.



4.1.1.5 Snow spectral albedo & BRDF

Performing a robust and accurate BRDF correction for snow using currently available methods is difficult because many different types of snow exist with widely varying reflectance anisotropy characteristics. Since a robust instantaneous BRDF correction is beyond our currently available capabilities, we have chosen to account for reflectance anisotropical effects using an empirical time-averaging treatment.

Our approach is based on the assumption that the directional-hemispherical reflectance (black-sky albedo) can be estimated with sufficient accuracy by sampling it from various viewing directions. By averaging the directional-directional reflectances of a snow site over a sufficient time-period (5 days or more), the resulting temporal average of snow albedo should be accurate even if the instantaneous directional-directional reflectances (instantaneous CLARA-SAL products) have significant BRDF-related under- and overestimations.

The retrieval method depends on sufficient sampling of the viewing hemisphere during the observation period. To demonstrate the achievable sampling, we show the sampled viewing zenith and azimuth angles during 2008 for the DYE-2 site on the Greenland Ice Shelf (66.48N, -46.28E) in Figure 16. The figure clearly shows how the viewing geometries of the retrievals are evenly distributed throughout the year. As it is a fair assumption that such distributions are similar at each longitude, we expect that similar distributions will occur over Canada and Northern Eurasia as well. As we approach the poles, the satellite retrieval density increases, further increasing the representativeness of our hemispherical reflectance sample and thus increasing the accuracy of the albedo estimate.

The method is most accurate during periods when the snow over a site experiences no significant changes. Melting and first snowfall periods will show a different BRDF signature over a site, and thus the estimated temporal means of albedo may suffer in accuracy. However, using our method, the albedo estimate is always based on the realized reflectances of the snow pack. Thus none of the inaccuracy results from an inappropriately chosen snow reflectance model for a scene.

 	EUMETSAT SAF on CLIMATE MONITORING Algorithm Theoretical Basis Document Surface Albedo CLARA-A1	Doc.No.: SAF/CM/FMI/ATBD/GAC/SAL Issue: 1.2 Date: 11.06. 2012
---	--	---

Distribution of Satellite Azimuth Viewing Angle and Viewing Zenith Angle per month during 2008 at DYE-2

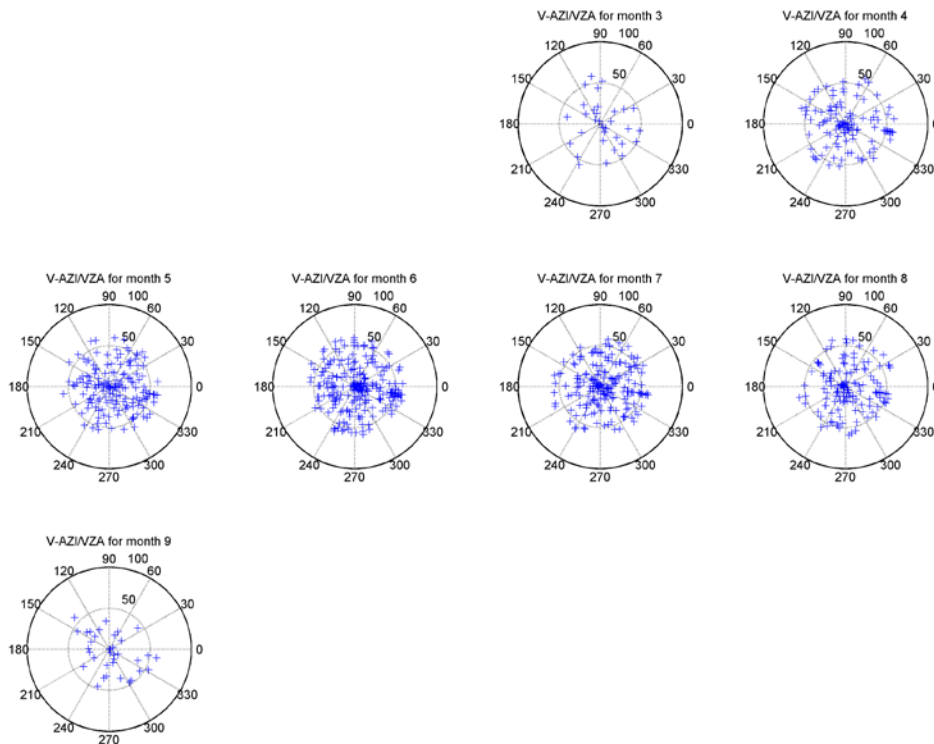




Figure 16: Satellite zenith and azimuth angles of successful CLARA-SAL retrievals during 2008 at DYE-2 in Greenland (66.48N, -46.28E). The polar plots show viewing (satellite) zenith angles in the radial axis and viewing azimuth angles in the angular axis.

4.1.1.6 Spectral conversion and SZA normalization

The last remaining stage in deriving the surface broadband albedo is the conversion from spectral directional albedo to broadband albedo. The instruments observing the radiances only pick up information in discrete spectral bands, such as the 0.58 - 0.68 μm red and 0.725 - 1 μm NIR wavelength channels of AVHRR (used for CLARA-SAL). Climatological applications for albedo require a total shortwave broadband albedo to be derived, so the observed spectral albedos must be extended to full shortwave spectral width. This is accomplished by the narrow-to-broadband conversion (NTBC) algorithm.

There are several NTBC algorithms employed in CLARA-SAL to account for all the surface types. The employed algorithms are based on the study results that atmospheric conditions do not significantly affect the conversion from narrow- to broadband albedo, and therefore linear regression may be used to extrapolate broadband albedo from the narrowband observations (Liang 2000). The methodology of deriving the regression coefficients may be found in the relevant publications.

Broadband surface albedo algorithms are usually limited by the sun zenith angle range that they can accept. For many surface types, the albedo of a scene with a large sun zenith angle becomes difficult to model due to extensive atmospheric scattering because of longer path lengths, as well as the irregularity of the scene BRDF at large sun zenith angles (van

 	EUMETSAT SAF on CLIMATE MONITORING Algorithm Theoretical Basis Document Surface Albedo CLARA-A1	Doc.No.: SAF/CM/FMI/ATBD/GAC/SAL Issue: 1.2 Date: 11.06. 2012
---	--	---

Leeuwen and Roujean 2002, DeAbreu et al. 1994). Similar limitations apply to satellite observations with large satellite zenith angles for similar reasons. As a result, CLARA-SAL omits all observations with larger SZA or VZA than a preprogrammed maximum. The assigned limits to SZA and VZA in CLARA-SAL are 70 degrees and 60 degrees, respectively.

CLARA-SAL employs the algorithm of Xiong et al. (2002) for snow, and water broadband albedo is determined from a LUT by Jin et al. (2004). For water pixels, this is the only relevant computation step since the actual observed reflectances are not used. For non-snow covered land surfaces, the algorithm by Liang (2000) is used for broadband conversion.

Since the SZA dependency of a snow pack has been shown to vary according to snow pack characteristics (Wang and Zender, 2011), a single normalization scheme for SZA dependency of snow albedo is not yet available. Therefore we omit this normalization at this time to avoid introducing artificial errors into the product. The realized SZA for land/snow pixels in the end products will correspond with the average SZA of the individual overpasses that consist the time averaged product. The processing limit for SZA remains at 70 degrees, thus providing an upper limit for the realized SZA of the products. An approximate realized SZA for scenes may be calculated by estimating the typical SZA range of variation for the latitude of the scene weighed by the overpass times of the satellites.

Since the CM SAF CLARA-SAL distributable products are the pentad and monthly means, the final step performed is the temporal averaging.. The currently used method is the arithmetic average of all instantaneous retrievals in a 0.25 degree end product pixel over the pentad/month in question.

4.1.2 Mathematical Description of the Algorithm

This chapter details the specific formulae and coefficients used in computing the CLARA-SAL instantaneous product. It is mostly for those interested in the details of CLARA-SAL product generation. Details that are irrelevant to the scientific accuracy of the product, such as statistics generation and user messaging, are omitted.

4.1.2.1 Cloud mask

Input: Observed radiances for AVHRR & auxiliary data.

Method: Not covered by this ATBD. The details on the AVHRR-PPS package and cloud mask derivation may be found at Dybbroe et al. (2005).

Output: Cloud mask image for CLARA-SAL.



4.1.2.2 Atmospheric correction

Input: TOA reflectances from the PPS preprocessing package, SMAC (continental) coefficients, SZA, VZA, differential sun-satellite azimuth angle, atmospheric water vapor (g/cm^2), atmospheric ozone (atm/cm), aerosol optical depth (dimensionless), atmospheric pressure (hPa).

Method: The SMAC algorithm is based on an inverse solution to the following atmospheric absorption/scattering equation (Rahman and Dedieu 1994, eq. 2)

$$\rho_{TOA}(\theta_s, \theta_v, \Delta\varphi) = t_g(\theta_s, \theta_v) \left\{ \rho_a(\theta_s, \theta_v, \Delta\varphi) + \frac{T(\theta_s)T(\theta_v)\rho(\theta_s, \theta_v, \Delta\varphi)}{1 - \rho(\theta_s, \theta_v, \Delta\varphi)S} \right\} \quad (14)$$

We solve the equation for the surface reflectance ρ

 	EUMETSAT SAF on CLIMATE MONITORING Algorithm Theoretical Basis Document Surface Albedo CLARA-A1	Doc.No.: SAF/CM/FMI/ATBD/GAC/SAL Issue: 1.2 Date: 11.06. 2012
---	--	---

$$\rho(\theta_s, \theta_v, \Delta\varphi) = \frac{\rho_{TOA} - t_g \rho_a(\theta_s, \theta_v, \Delta\varphi)}{t_g T(\theta_s) T(\theta_v) + \rho_{TOA} - t_g \rho_a(\theta_s, \theta_v, \Delta\varphi) S} \quad (15)$$

where

ρ_{TOA} = Reflectance at the top of the atmosphere

t_g = Total gaseous transmission (both upward and downward paths)

ρ_a = Atmospheric reflectance, a function of the optical properties of air molecules and aerosols as well as the illumination/viewing geometry

$T(\theta_s)$ = Atmospheric (scattering) transmission (downward)

$T(\theta_v)$ = Atmospheric (scattering) transmission (upward)

S = Spherical albedo of the atmosphere

The gaseous transmission term is

$$t_g = e^{a(mU)^n} \quad (16)$$

where a and n are predefined constants (but different for each gas). The transmission is calculated separately for ozone, water vapour, oxygen, carbon dioxide, methane, nitrogen dioxide, and carbon monoxide. Total gaseous transmission in eq. 15 is the sum of all these components. All constants in the calculations are available from the CESBIO website, <http://www.cesbio.ups-tlse.fr/us/serveurs4.htm>. U is the vertically integrated absorber amount, and m is the airmass ($1/\cos(\theta_s) + 1/\cos(\theta_v)$).

The atmospheric reflectance ρ_a is

$$\rho_a = \rho_{ar} + \rho_{ap} - R_{ar} - R_{ap} - R_{\delta s} \quad (17)$$

In other words, the total atmospheric reflectance is a sum of the atmospheric reflectances resulting from Rayleigh and aerosol scattering processes. The sum is then corrected by a subtraction of residuals to account for numerical inaccuracies.

The Rayleigh atmospheric reflectance is defined as

$$\rho_{ar} = \frac{\tau_r p_r(\xi)}{4 \cos(\theta_s) \cos(\theta_v)} \quad (18)$$

The molecular optical depth τ_r is a predefined constant, but it is corrected for surface pressure variations by

$$\tau_r(P) = \tau_r(P_0) \frac{P}{P_0} \quad (19)$$


The molecular phase scattering function p_r is calculated assuming a molecular depolarisation factor $\delta=0.0139$

$$p_r(\xi) = 0.7190443(1 + \cos^2(\xi)) + 0.0412742 \quad (20)$$

where the scattering angle cosine is calculated by

$$\cos(\xi) = -(\cos(\theta_s) \cos(\theta_v) + \sqrt{(1 - \cos^2(\theta_s))(1 - \cos^2(\theta_v))} \cos(\Delta\varphi)) \quad (21)$$

The aerosol atmospheric reflectance requires more complicated calculations. To condense the equations, we first define $\mu_s = \cos(\theta_s)$ and $\mu_v = \cos(\theta_v)$. The aerosol atmospheric reflectance is

	EUMETSAT SAF on CLIMATE MONITORING Algorithm Theoretical Basis Document Surface Albedo CLARA-A1	Doc.No.: SAF/CM/FMI/ATBD/GAC/SAL Issue: 1.2 Date: 11.06. 2012
---	--	---

$$\rho_{ap} = \frac{1}{\mu_s \mu_v} \left\{ \begin{array}{l} \frac{X \mu_v}{1 + \kappa \mu_v} (1 - e^{-\frac{\tau_p (1 + \kappa \mu_v)}{\mu_v}}) + \frac{Y \mu_v}{1 + \kappa \mu_v} (1 - e^{-\frac{\tau_p (1 + \kappa \mu_v)}{\mu_v}}) \\ + (Z + P(\xi)) \frac{\mu_s \mu_v}{\mu_s + \mu_v} (1 - e^{-\tau_p (\frac{1}{\mu_s} + \frac{1}{\mu_v})}) \end{array} \right\} \quad (22)$$

where

$$\begin{aligned} \kappa^2 &= (1 - \omega_0)(3 - \omega_0 \beta_1) \\ \beta_1 &= 3g \end{aligned} \quad (23)$$

g is the asymmetry factor and ω_0 is the single scattering albedo of the atmosphere. Both are pre-defined constants loaded from SMAC coefficient file. The average aerosol optical depth (for both AVHRR spectral bands) is calculated from the aerosol optical depth at 550nm (input) by

$$\tau_p = a_0 + a_1 \tau_{550} \quad (24)$$

where a_0 and a_1 are predefined constants.

The coefficients X , Y , and Z are complicated numerical functions of the asymmetry factor, single scattering albedo, and the viewing geometry. The calculations are listed in Appendix B.

The residuals are calculated as follows. Firstly the Rayleigh residual is

$$R_{ar} = rr1 + \frac{rr2 * p_r(\xi) * ta * \frac{P}{P_0}}{\mu_s \mu_v + rr3 * \left(\frac{(ta * \frac{P}{P_0} * p_r(\xi))}{\mu_s \mu_v} \right)^2} \quad (25)$$


where $rr1, rr2, rr3$ and ta are predefined constants from the SMAC coefficient file.

The aerosol residual is

$$R_{ap} = ra1 + ra2 * (\tau_p * m * \cos(\xi)) + ra3 * (\tau_p * m * \cos(\xi))^2 + ra4 * (\tau_p * m * \cos(\xi))^3 \quad (26)$$

where $ra1, ra2, ra3$ and $ra4$ are predefined constants from the SMAC coefficient file.

Finally, the 6S residual is

	EUMETSAT SAF on CLIMATE MONITORING Algorithm Theoretical Basis Document Surface Albedo CLARA-A1	Doc.No.: SAF/CM/FMI/ATBD/GAC/SAL Issue: 1.2 Date: 11.06. 2012
---	--	---

$$R_{6S} = rs1 + rs2 * ((\tau_p + ta * \frac{P}{P_o}) * m * \cos(\xi)) + rs3 * ((\tau_p + ta * \frac{P}{P_o}) * m * \cos(\xi))^2 + rs4 * ((\tau_p + ta * \frac{P}{P_o}) * m * \cos(\xi))^3 \quad (27)$$

where rs1, rs2, rs3, rs4 and ta are predefined constants from the SMAC coefficient file.

The atmospheric transmission terms T are defined as

$$T(\theta_x) = a_0 + \frac{a_1 \tau_{550}}{\cos(\theta_x)} + \frac{a_2}{1 + \cos(\theta_x)} \quad (28)$$

where the a-coefficients are predefined in the SMAC coefficient file.

The last term in the atmospheric correction is the spherical albedo of the atmosphere, given by

$$S = 1 - \frac{1}{(b_0 + b_1 \tau_{550})} \quad (29)$$

where b₀ and b₁ are predefined constants from the SMAC coefficient file.

Finally, it should be mentioned that the aforementioned method assumes that the corrected area is large enough that neighbouring area effects on the correction are negligible. According to Rahman and Dedieu, 1km pixel size is sufficient for this. The GAC pixel is much larger and therefore this assumption appears valid. The reader is also reminded that the SMAC coefficient files are both satellite and channel-specific.

Output: Surface reflectances of non-snow land surfaces.

4.1.2.3 BRDF correction & spectral albedo computation

Input: Surface reflectances from atmospheric correction, SZA, VZA, differential sun-satellite azimuth angle, surface type.


Method: Locate surface type from USGS, calculate NDVI for AVHRR ch1 and ch2 reflectances. If NDVI of pixel is < 0.1, surface is "Barren". For snow pixels, see section 4.1.1.5.

Obtain BRDF kernel values for appropriate surface type, used kernel values are in Table 3 (Wu et al. 1995). Then compute the normalized surface reflectances (as a multiple of nadir reflectance) with eqs. 30 and 31. The function dependencies have been omitted here for clarity. Overall, the normalized surface reflectances depend on the sun and viewing zenith angles, the azimuth difference angle between sun and satellite, the surface type and NDVI. The equation was introduced in section 4.1.1.4 (eq. 8), and reiterated here for clarity for both AVHRR channels (1 and 2):

$$\Omega_{RED} = 1 + a_{11}f_1 + a_{21}f_2 \quad (30)$$

$$\Omega_{NIR} = 1 + a_{12}f_1 + a_{22}f_2 \quad (31)$$

where

	EUMETSAT SAF on CLIMATE MONITORING	Doc.No.: SAF/CM/FMI/ATBD/GAC/SAL
	Algorithm Theoretical Basis Document	Issue: 1.2
	Surface Albedo CLARA-A1	Date: 11.06. 2012

$$f_1 = \frac{1}{2\pi} * [(\pi - \varphi) * \cos(\varphi) + \sin(\varphi)] * \tan(\theta_s) * \tan(\theta_v) - \frac{1}{\pi} * \left(\tan(\theta_s) + \tan(\theta_v) + \sqrt{\tan(\theta_s)^2 + \tan(\theta_v)^2 - 2 * \tan(\theta_s) * \tan(\theta_v) * \cos(\varphi)} \right) \quad (32)$$

and

$$f_2 = \frac{4}{3\pi(\cos(\theta_s) + \cos(\theta_v))} \left[\left(\frac{\pi}{2} - \xi \right) \cos(\xi) + \sin(\xi) \right] - \frac{1}{3} \quad (33)$$

$$\xi = \cos(\theta_s)\cos(\theta_v) + \sin(\theta_s)\sin(\theta_v)\cos(\varphi) \quad (34)$$

Table 3: Kernel coefficients used in CLARA-SAL BRDF correction computation. Coefficients are land cover specific. Coefficients a_{x1} are for red channel, a_{x2} are for NIR channel. (Wu et al. 1995).

Scene type	a_{11}	a_{21}	a_{12}	a_{22}
Barren	0.21	1.629	0.212	1.512
Cropland	0	$3.622 * \text{NDVI}^{0.539}$	0	$1.62 * \text{NDVI}^{0.109}$
Forest	0	$3.347 * \text{NDVI}^{0.153}$	0	$1.830 * \text{NDVI}^{-0.105}$
Grassland	$1.335 * e^{-11.39 * \text{NDVI}}$	$-0.493 + 14.94 * \text{NDVI} - 18.32 * \text{NDVI}^2$	$7.745 * e^{-22.8 * \text{NDVI}}$	$-0.250 + 13.88 * \text{NDVI} - 20.43 * \text{NDVI}^2$

where the angles $\theta_s, \theta_v, \varphi$ are the satellite image's sun zenith, viewing zenith and relative azimuth angles, respectively. Next, the BRDF is computed a second time for the normalized viewing and illumination geometry, i.e. nadir view and zenith sun $\rightarrow \Theta_s = 0, \Theta_v = 0$. By dividing the BRDFs we get the normalization factor which is then used to multiply the surface reflectance to get the anisotropy-corrected & normalized surface reflectance (Wu et al. 1995).



$$\rho_{RED}(0,0,\varphi) = \frac{\Omega_{RED}(0,0,\varphi)}{\Omega_{RED}(\theta_s,\theta_v,\varphi)} * \rho_{RED}(\theta_s,\theta_v,\varphi) \quad (35)$$

$$\rho_{NIR}(0,0,\varphi) = \frac{\Omega_{NIR}(0,0,\varphi)}{\Omega_{NIR}(\theta_s,\theta_v,\varphi)} * \rho_{NIR}(\theta_s,\theta_v,\varphi) \quad (36)$$

Now we have BRDF-corrected surface reflectances, normalized to a common viewing and illumination geometry. The next step produces hemispherical spectral surface albedo images for both red and NIR wavebands. The equations for this are eqs. 10-12, locating the a-coefficients from Table 3. with the NDVI constraint, and keeping in mind that these coefficients deal with nadir-multiple hemispherical albedos. To get the actual absolute value, we multiply the nadir-normalized surface reflectance with the BRDF kernels as in eq. 10. So, the hemispherical albedos are

$$\alpha_{RED}(\theta_s) = \rho_{RED}(0,0,\varphi) * (1 + a_{11}I_1 + a_{21}I_2) \quad (37)$$

$$\alpha_{NIR}(\theta_s) = \rho_{NIR}(0,0,\varphi) * (1 + a_{12}I_1 + a_{22}I_2) \quad (38)$$

 	EUMETSAT SAF on CLIMATE MONITORING Algorithm Theoretical Basis Document Surface Albedo CLARA-A1	Doc.No.: SAF/CM/FMI/ATBD/GAC/SAL Issue: 1.2 Date: 11.06. 2012
---	--	---

Output: BRDF-corrected spectral red and NIR surface albedos normalized to nadir view, sun zenith geometry.

4.1.2.4 Spectral conversion from narrow to broadband and view normalization

Input: spectral red and NIR surface albedos.

Method: The last stage in deriving the broadband surface albedo product from the satellite observation is the conversion from spectral albedos to full broadband. The most common method for this is a straightforward weighted linear combination of the spectral albedos, as shown by several studies (van Leeuwen and Roujean 2002, Xiong et al. 2002, Liang 2000, Song and Gao 1999, and references therein).

CLARA-SAL chooses the linear combination method according to sensor and surface type. For all non-snow land surfaces observed by an AVHRR, the broadband albedo is computed following an narrow-to-broadband conversion (NTBC) approach by Liang (2000). The NTBC is

$$\alpha = -0.3376 \cdot \alpha_{RED}^2 - 0.2707 \cdot \alpha_{NIR}^2 + 0.7074 \cdot \alpha_{RED} \cdot \alpha_{NIR} + 0.2915 \cdot \alpha_{RED} + 0.5256 \cdot \alpha_{NIR} + 0.0035 \quad (39)$$

For any snow/sea ice pixels (identified by cloud mask snow/ice flag over ocean pixels), the method follows Xiong et al. (2002). The equation is as follows:

$$\alpha = 0.28(1 + 8.26\Gamma)\alpha_{RED} + 0.63(1 - 3.96\Gamma)\alpha_{NIR} + 0.22\Gamma - 0.009 \quad (40)$$

where



$$\Gamma = \frac{\alpha_{RED} - \alpha_{NIR}}{\alpha_{RED} + \alpha_{NIR}} \quad (41)$$

Again, the reader is reminded that the chosen empirical-temporal BRDF correction method implies that the output of the NTBC algorithm at the instantaneous image level is a bidirectional surface reflectance, which the temporal averaging (may be thought of as a coarse integration over the viewing hemisphere) converts into a directional-hemispherical reflectance (or black-sky albedo).

For any water pixels not covered by sea ice, the broadband albedo is retrieved from a LUT. The applied LUT is by Jin et al. (2004). The LUT has 8400 records and therefore cannot be displayed here, but in general the retrieved broadband ocean albedo depends on four pixelwise parameters:

1. Sun Zenith Angle (SZA)
2. wind speed, CLARA-SAL default = 10 m/s
3. aerosol optical depth (AOD), CLARA-SAL default = 0.1
4. ocean chlorophyll content, CLARA-SAL default = 0.15 mg/m³

The LUT has been formed by fitting Coupled Ocean-Atmosphere Radiative Transfer (COART) model runs to concurrent radiation and environmental observations at the NASA CERES Ocean Validation Experiment (COVE) site (Chesapeake Bay, USA). The COART model has been described in detail by Jin et al. (2006). The COART model treats both atmosphere and ocean as a single system where ocean layers simply have different optical characteristics. The model calculates scattering and absorption processes (by air and water molecules, aerosols, and clouds) in the atmosphere and in the ocean. Surface roughness effects of the ocean surface are explicitly included and calculated.


 	<p align="center">EUMETSAT SAF on CLIMATE MONITORING</p> <p align="center">Algorithm Theoretical Basis Document Surface Albedo CLARA-A1</p>	<p>Doc.No.: SAF/CM/FMI/ATBD/GAC/SAL</p> <p>Issue: 1.2</p> <p>Date: 11.06. 2012</p>
---	--	--

At present, CLARA-SAL processing has no access to realtime wind speed, AOD or chlorophyll content data, so default constants are used. Therefore the modeled ocean albedo depends in principle only on the SZA. However, since all distributed CLARA-SAL products are normalized over ocean to a SZA of 60 degrees (see below), all ocean albedo pixels have in fact a constant value of ~ 0.068 . A similar SZA normalization over land is not implemented in this first CLARA-SAL Edition. The effect on albedo is typically 0.01 – 0.02. Since snow SZA dependency is more difficult to model, the product retains better homogeneity without such a normalization. The intent is to include the SZA normalization over land and snow (if feasible) in the next CLARA-SAL Edition.

In principle we have now computed the surface broadband albedo for a single satellite image.

The CLARA-SAL computation is now finished. The pentad and monthly mean products are composited by a pixel-by-pixel averaging of all valid albedo values over the instantaneous images.

Output: Instantaneous broadband surface albedo product. Bidirectional broadband reflectance for snow pixels in the instantaneous CLARA-SAL images. Broadband surface albedo of snow in the temporally averaged products.

	EUMETSAT SAF on CLIMATE MONITORING Algorithm Theoretical Basis Document Surface Albedo CLARA-A1	Doc.No.: SAF/CM/FMI/ATBD/GAC/SAL Issue: 1.2 Date: 11.06. 2012
---	--	---

4.1.3 Error Budget Estimates

The objective of the CLARA-SAL product is to describe the broadband surface albedo of Earth's surface to a degree of accuracy of 25% (relative). Due to the complex, multistage computation process required to obtain the surface albedo product, there are several error sources that may propagate through the production chain. The error sources and their estimated relative effect is shown in Table 4. It should be stressed that the values are estimates based on the algorithm literature and simulations of the behaviour of the CLARA-SAL code with input data modified to reflect sources of inaccuracy. Information on the actual achieved accuracy is obtainable from the Validation Report [AD-2].



Table 4: Estimates of error sources and their effects on the instantaneous CLARA-SAL product. All values are in relative albedo (percent).

Error type \ Instrument and scene type	AVHRR land	AVHRR Snow & ice
SMAC errors from coeff. and aux-data	0-4% (over desert 0-8%)	0-4% (assumed)
LUC inaccuracies	0-5%	none assumed
BRDF errors	0-5%	unknown
NTBC inaccuracy	0-10%	0-10%
Total	0-24% for the known error sources	0-14% for the known error sources
Over desert	0-28%	

The correctness of the cloud mask is essential for the accuracy of the CLARA-SAL product. Cloud underestimation may lead to albedo retrieval errors of more than 50 %. While the current cloud mask is sophisticated and not prone to such errors, the user should be aware that there is a higher risk that the cloud mask accuracy affects CLARA-SAL in coastal areas and over snow-covered terrain. The cloud mask hit rate over snow-covered regions in the Arctic has been validated as roughly 90% during polar summer when CLARA-SAL is retrievable (Karlsson and Dybbroe, 2010)

The SMAC coefficients used for atmospheric correction are different for continental areas and desert due to the heavy aerosol loading over desert areas. However, CLARA-SAL does not currently delineate between barren and desert areas (e.g. tundra and desert), so continental SMAC correction is applied to all pixels. In addition, to be fully accurate SMAC requires pixelwise data on water vapour content, integrated ozone amount, AOD at 550 nm, and pressure at surface level. This Edition of CLARA-SAL has access to only the water vapour and surface pressure data on a continuous basis, program defaults are used for ozone amount (0.35 atm/sq. cm) and AOD (0.1). Simulations on the effect of SMAC coefficient type and changing AOD conditions over typical arid pixels in North Africa show that the expected error from the use of continental aerosol model is approximately 0 - 4 % (relative) in broadband albedo when AOD at 550 nm changes between 0.1 and 0.4, respectively.

Recently, Proud et al. (2010) proposed a correction to the SMAC algorithm for SEVIRI. Their study results showed that the SMAC algorithm for SEVIRI may suffer from considerably low accuracy when the solar zenith angle over a scene exceeds 30 degrees. Their proposed changes to the algorithm add only a minor additional CPU load, while improving the correction results over their African test sites. They also state that a similar correction would improve the SMAC accuracy on other instruments. Based on the results of their study, CLARA-SAL users should also be aware of additional potential uncertainties within the SMAC correction algorithm.

 	EUMETSAT SAF on CLIMATE MONITORING Algorithm Theoretical Basis Document Surface Albedo CLARA-A1	Doc.No.: SAF/CM/FMI/ATBD/GAC/SAL Issue: 1.2 Date: 11.06. 2012
---	--	---

The land use classification information is needed by several CLARA-SAL processing steps to assign BRDF kernels and separate ocean and permanent snow/ice areas, among other things. Man-made changes in LUC may cause poor matches between assigned BRDF and actual reflectance behaviour, resulting in a retrieval error for the albedo. Oceans, barren areas and snow/ice do not generally suffer from man-made changes for obvious reasons, but other misclassifications such as cropland portrayed as forest due to an outdated LUC dataset may occur. We have studied the computed albedo changes resulting from different LUC datasets, and the results indicate that the probable error is in the order of 0 - 5 % relative for land surfaces. However, as a single LUC dataset is used for the 27-year period, larger regional differences may be found as natural and man-made changes in the landscape occur.

BRDF errors are a potential factor in the retrieval accuracy of CLARA-SAL. Incomplete understanding of the reflectance properties of natural targets is a difficult thing to estimate, so the range of probable inaccuracy for this factor is also large enough to be considered. The values obtained for the estimated error are from the relevant algorithm publications using typical surface broadband albedo values.

Inaccuracies may also arise from the need to compress USGS classes into the internal CLARA-SAL LUC types, as in Table 1. This likely causes some BRDF inaccuracies for different forest types or marshlands. However, over the generally heterogeneous 0.25 degree resolution of the end user products their contribution is estimated to be minor.

Because the BRDF correction for snow is treated with an empirical temporal averaging scheme, the under- or overestimations of individual CLARA-SAL retrievals is very difficult to estimate. The overall accuracy of this CLARA-SAL algorithm for snow albedo retrievals over the Greenland Ice Sheet and Arctic Ocean in 2007 has been discussed in a publication by Riihelä et al. (2010). They found the overall accuracy of CLARA-SAL over snow surfaces to be between 5-10% (relative) in most cases where drastic snowmelt or topography did not degrade the algorithm performance. More details on the CLARA-SAL behaviour over snow and ice may be found in (AD-2).

The Narrow-to-Broadband-Conversion (NTBC) inaccuracies listed here are derived directly from the publications describing the algorithms. The interested reader should see Xiong et al. (2002), and Liang (2000) for details.

This Edition of CLARA-SAL is not normalized for a common Sun Zenith Angle for land and snow/ice surfaces. While this does not constitute a retrieval error in itself, the products will show a somewhat larger degree of variability in the temporal means as a result. The variability is typically on the order of 0.01 to 0.02.

A topography correction has been applied to this Edition. There is currently insufficient data to estimate the effectiveness of the correction, therefore we do not offer such numbers here. Based on the theoretical studies (see Section 4.1.1.2 for discussion), we expect at least a 10% (relative) improvement in accuracy over mountainous areas (over 5 degree mean slope). The true effect will be studied in future validation work.

4.2 SMAC atmospheric correction sensitivity study

To assess the effects of applying constant aerosol and O₃ inputs in the atmospheric correction, we have performed a sensitivity study. The study was carried out by simulating SMAC-correction and the SAL algorithm using different simulated terrain types and AOD/O₃ loading. The simulated cases and the results are as follows:

CASE 1: Vegetation with a favorable viewing geometry

Grass target, VIS & NIR channel on AVHRR/3. Set VZA=SZA=45 deg., RELAZ=90 deg., H20=2.5, pre=1013, utilize NOAA16 correction coefficients.

We simulate AOD (at 550nm) variation between 0.05 and 0.4 with 0.01 interval while O3=0.35. Set VIS TOA reflectance to 0.12 and NIR TOA reflectance to 0.35.

Results:

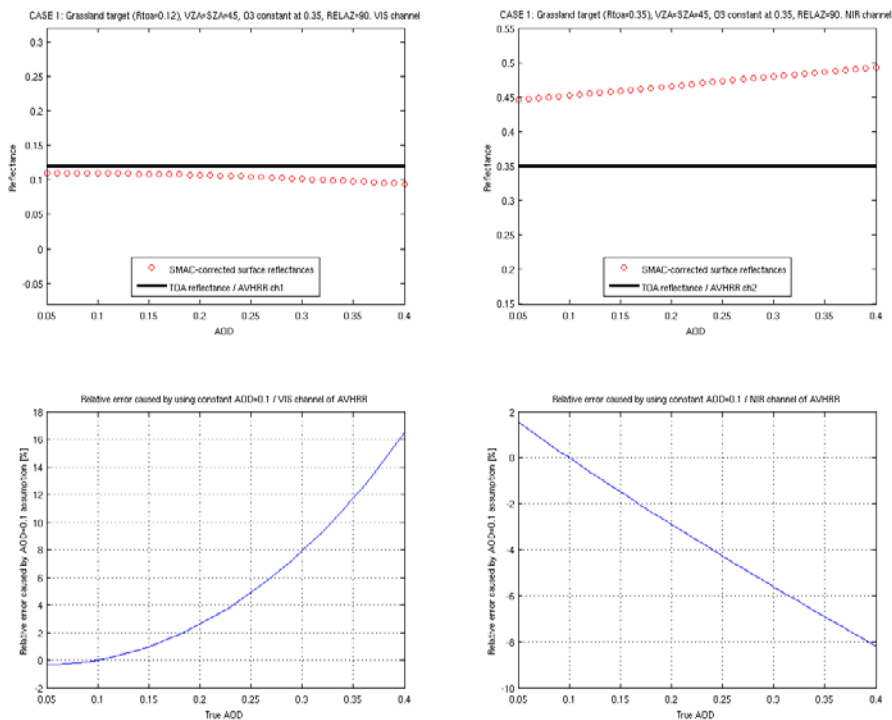


Figure 17: SMAC correction effect (above) and relative retrieval error caused by an assumption of AOD=0.1 (below) for grassland at VIS channel with R_{toa}=0.12 (left) and at NIR channel with R_{toa}=0.35 (right). SZA=VZA=45 degrees.

With the assumed R_{toa} reflectances, assumption of AOD=0.1 causes errors smaller than 5% relative while true AOD is below 0.25 (for both VIS and NIR channels). Retrieval error for surface reflectance at VIS channel grows substantially at high AOD values of 0.35 and above. How common are AOD values above 0.25?

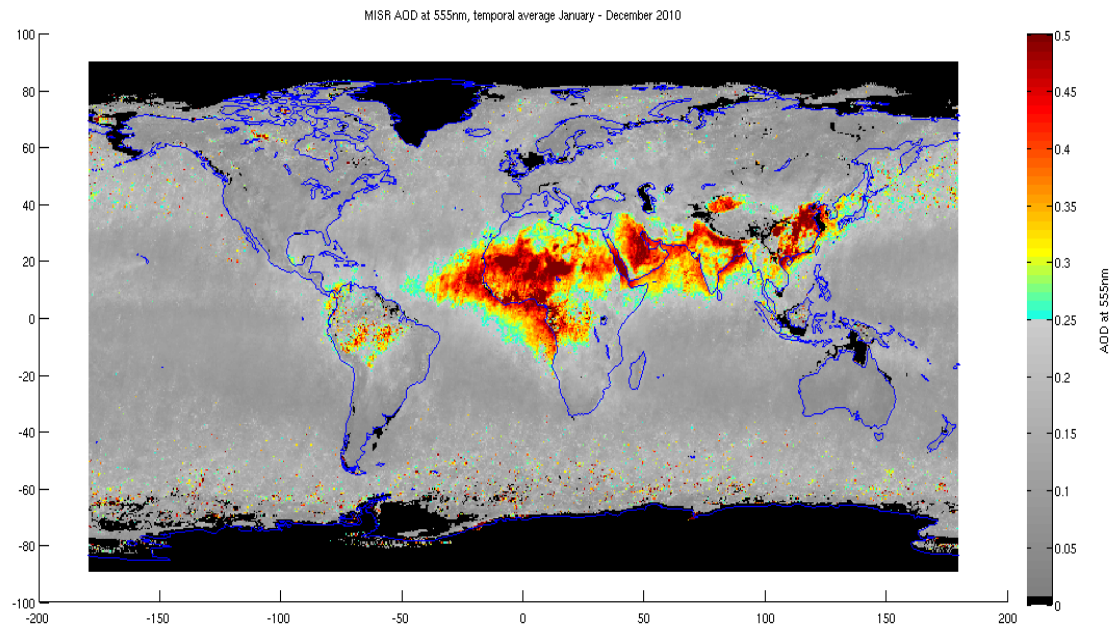


Figure 18: MISR average AOD at 555nm between January-December 2010

Figure 18 shows the MISR average AOD at 555nm between January and December 2010, retrieved from the NASA Giovanni system. The color scale has been chosen to highlight regions where average AOD is above 0.25. As we can see, over most land masses of the Northern Hemisphere the AOD is below 0.25. Exceptions are Sahara, Arabian Peninsula, Indian subcontinent, China and some other smaller regions in East and Southeast Asia, along with some areas of the Amazon. The AOD product from MODIS/Terra over the same period has been checked also and is principally in agreement with the MISR product.

CASE 2: Vegetation with an unfavorable viewing geometry

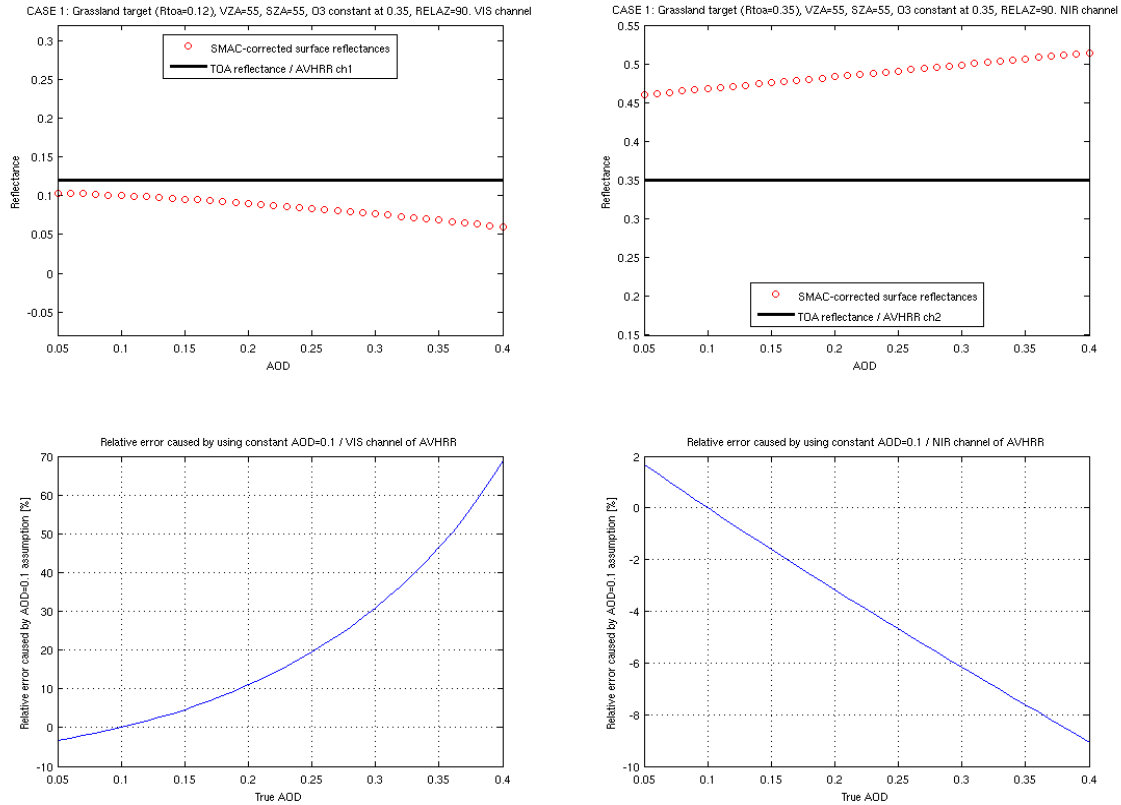


Figure 19: SMAC correction effect (above) and relative retrieval error caused by an assumption of AOD=0.1 (below) for grassland at VIS channel with $R_{toa}=0.12$ (left) and at NIR channel with $R_{toa}=0.35$ (right). $SZA=VZA=55$ degrees.

Same conditions as in case 1, except setting VZA and SZA to 55 degrees (more unfavorable geometry case)

Results:

VIS channel retrieval error increases sharply as imaging geometry becomes unfavorable. AOD estimation error of 0.05 is sufficient to cause a 5% retrieval error in surface reflectance in the VIS channel. NIR channel remains fairly insensitive to AOD estimation error.

The effect appears dramatic, but to fully understand the significance in the end product (CLARA-SAL), we need to simulate the entire production process from the atmospheric correction to instantaneous broadband black-sky albedo. We have done so with the following results.

For our example case ($R_{TOA_VIS}=0.12$, $R_{TOA_NIR}=0.35$, $SZA=VZA=55$ degrees, $RELAZ=90$ degrees), given fixed atmospheric inputs with $AOD=0.1$, the instantaneous broadband black-sky albedo is 0.248. If we increase AOD to 0.15 while keeping all other inputs constant, the albedo changes to 0.246 (-0.81%). A large increase to AOD to 0.3 while keeping other inputs constant produces an albedo of 0.235 (-5.24%). This is physically easy to understand; for vegetation, the total broadband reflectance is dominated by the NIR

waveband where an AOD increase/decrease produces a weaker response in the atmospheric correction (in comparison to the VIS waveband).

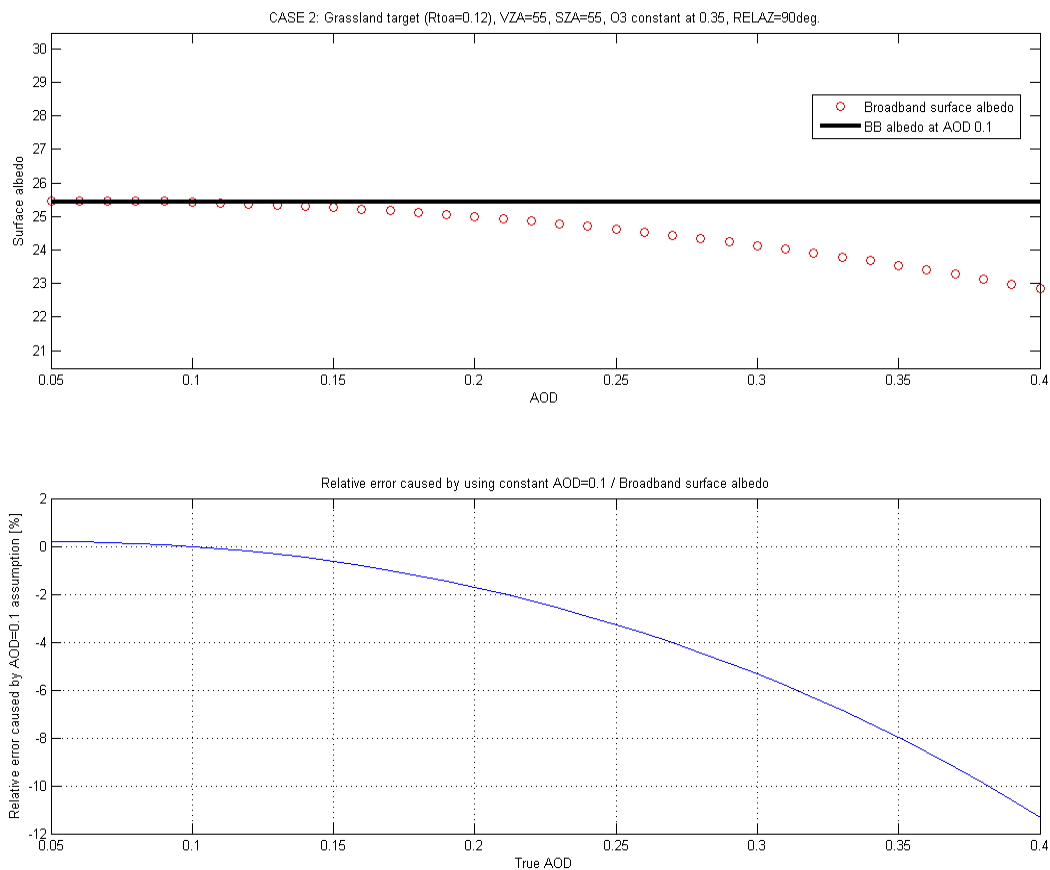


Figure 20: The impact of using a constant AOD on the resulting broadband albedo in Case 2. Above: the calculated broadband albedo using various AOD values in the atmospheric correction. Below: Relative error in the broadband albedo calculated using AOD=0.1 relative to using a ‘true’ AOD value.

Figure 20 illustrates the AOD assumption impact on albedo in graphical form. The impact remains quite small when $AOD < 0.2$. The impact also diminishes when the viewing geometry is more favorable. When SZA and VZA are less than 20 degrees, the simulations of Case 1 show an impact between -1% to +4% in the demonstrated AOD range of 0.05 to 0.4, respectively.

CASE 3: Desert

Desert target, VIS & NIR channel on AVHRR/3. Set VZA=30, SZA=45 deg., RELAZ=40 deg., H2O=2.5, pre=1013, utilize NOAA16 correction coefficients.

- Simulate AOD (at 550nm) variation between 0.05 and 0.4 with 0.01 interval while O3=0.35.
- Set VIS TOA reflectance to 0.32 and NIR TOA reflectance to 0.35, typical for e.g. Sahara desert reflectances.

CASE 3: Desert target ($R_{toa_{vis}}=0.32$), $VZA=30$, $SZA=45$, O_3 constant at 0.35, $RELAZ=40$ deg. CASE 3: Desert target ($R_{toa_{nir}}=0.35$), $VZA=30$, $SZA=45$, O_3 constant at 0.35, $RELAZ=40$ deg.

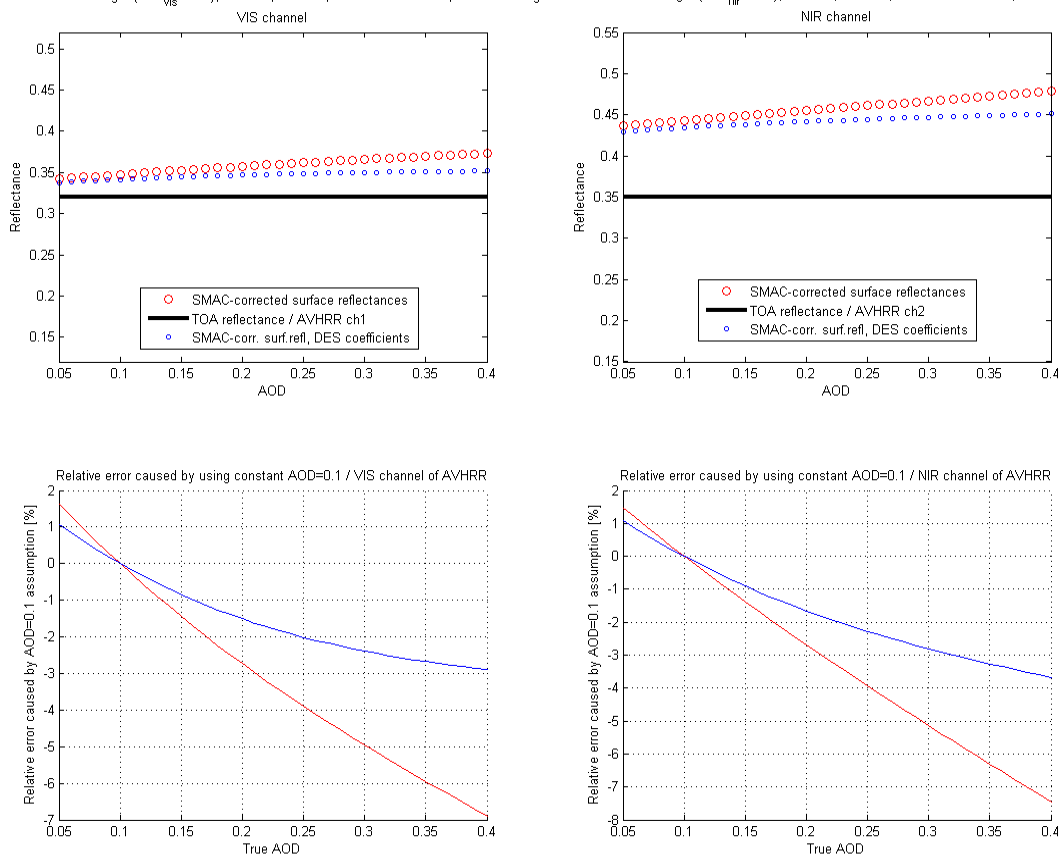


Figure 21: SMAC correction effect (above) and relative retrieval error caused by an assumption of AOD=0.1 (below) for a desert target at VIS channel with $R_{toa}=0.32$ (left) and at NIR channel with $R_{toa}=0.35$ (right). $SZA=35$, $VZA=45$ degrees. $RAZI=40$ deg. Blue curves show the correction effect if desert SMAC coefficients are used instead of continental ones.

Analysis:

Over desert targets with a favorable viewing geometry the AOD effect is quite linear and its magnitude is not dramatic. On the other hand, large AOD values occur more often so that the typical retrieval error in VIS and NIR surface reflectances can be ~5% relative. Considering the effect on broadband albedo, simulated SAL normalized to SZA 60 deg using the inputs above is **0.338**. Increasing AOD to 0.3 while keeping all other inputs constant increases the normalized broadband albedo to **0.357**. The relative difference is **5.5%**. This holds for the continental SMAC coefficients currently used. Correction using the desert-coefficients appears to depend less on the AOD.

It should be noted that the atmospheric correction magnitude depends not only on the AOD at 550nm, but also on the surface target brightness and the illumination/viewing angle geometry between the Sun and the observer. An example of this relationship is shown in Figure 22.

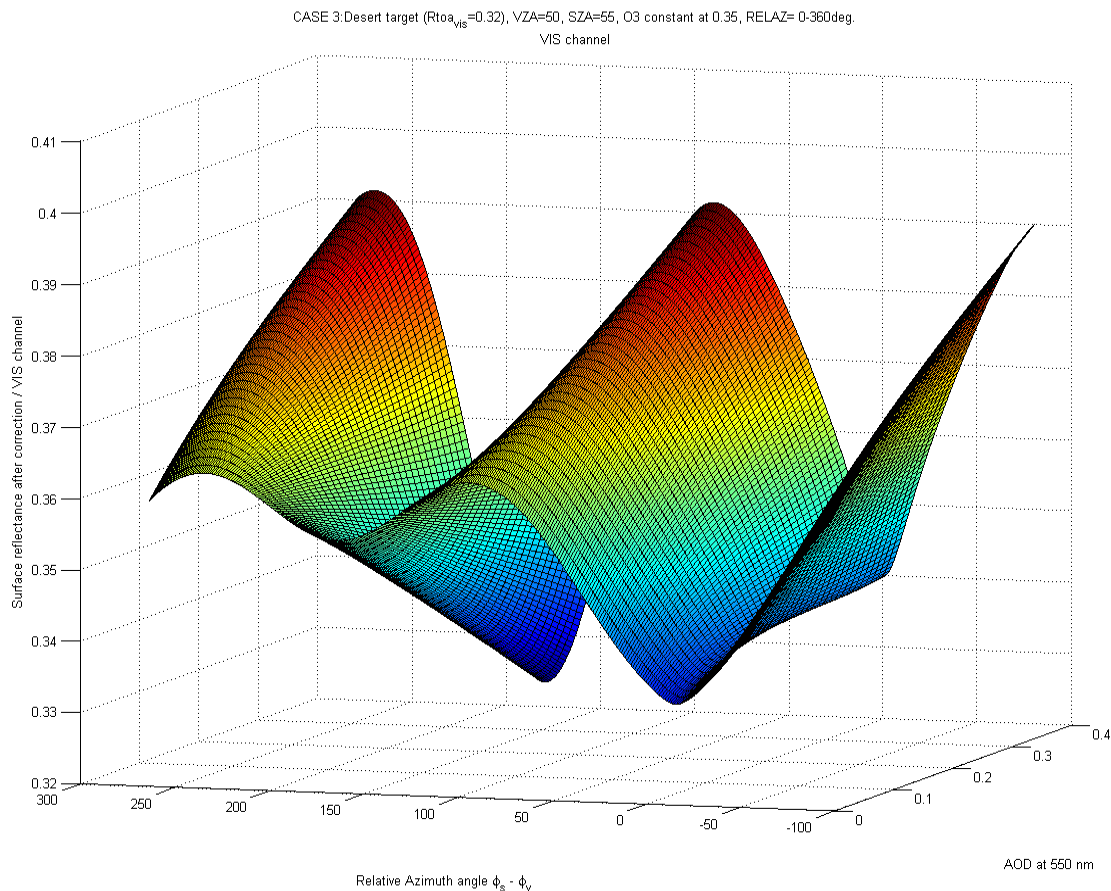


Figure 22: SMAC correction as a function of AOD and Relative Azimuth Angle. Correction magnitude shown for a desert target ($R_{toa}=0.32$) with continental coefficients as in SAL computation. O_3 concentration constant at 0.35, $SZA=55$, $VZA=50$ degrees.

When aerosol concentration is low, molecular scattering and absorption dominates. As the aerosol concentration increases, either aerosol scattering processes dominate (over dark targets) or aerosol absorption dominates (over bright targets) (Kaufman and Tarré, 1996). Thus the correction will either increase or decrease the corrected surface reflectance relative to the TOA reflectance. Over a bright target such as a desert, the correction increases the surface reflectance to compensate for the dominant absorption effect, and vice versa over darker vegetation targets at visible wavelengths. The viewing geometry also plays its role, as the atmospheric path length increases when SZA and/or VZA are large and the correction becomes larger. The relative azimuth angle between Sun and observer is also important, as the scattering processes between sunlight and atmospheric constituents have anisotropic characteristics. More specifically, molecular backscattering is very weak, whereas aerosol backscatter is relatively much stronger. Both scattering processes prefer small scattering angles, leading to the “wave-like” structure of the correction magnitude seen in Figure 22. As mentioned, the aerosol effects become dominant over molecular scattering at large AOD, which is why the rate of change in the correction magnitude is of opposite signs in the forward and backscattering directions.

CASE 4: Ozone effect evaluation

We also briefly evaluate the effect of applying a constant O₃ to the atmospheric correction. We test the effect on our Case 1 data, setting AOD to the SAL constant of 0.1. Thus the simulation set-up is

- a) Simulate O₃ variation between 0.1 and 0.8 with 0.01 interval while AOD=0.1. Set VIS TOA reflectance to 0.12 and NIR TOA reflectance to 0.35. SZA=VZA=45 degrees. RELAZ=90 degrees.

Results:

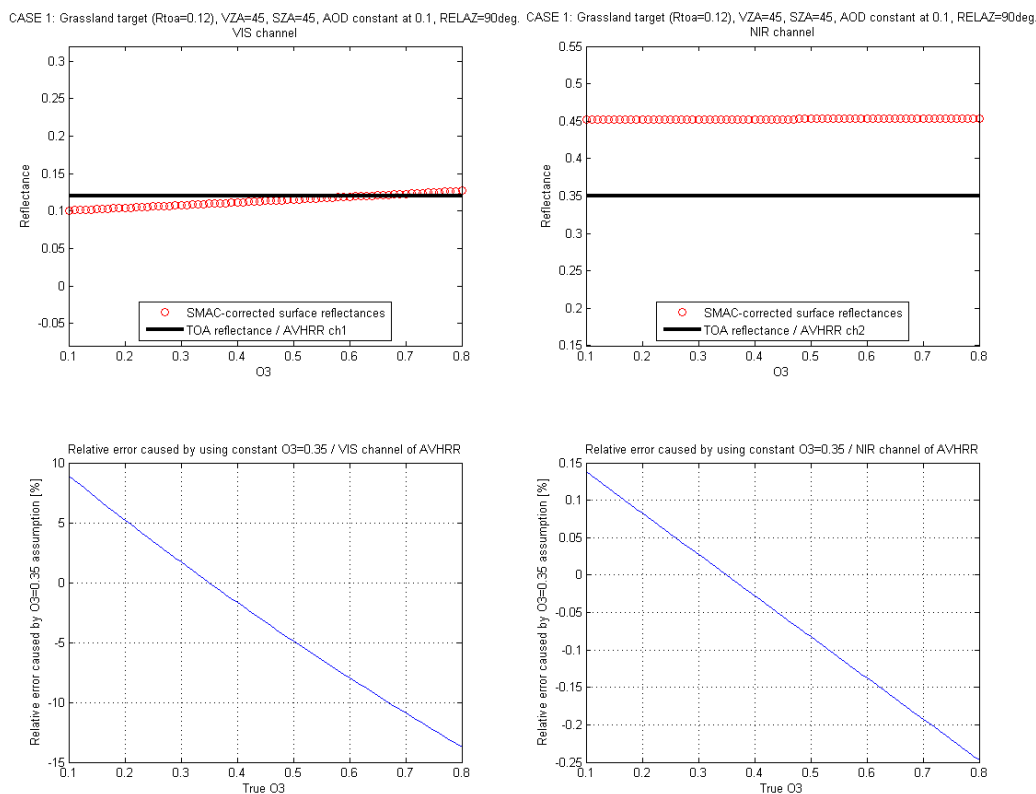


Figure 23: SMAC correction effect (above) and relative retrieval error caused by an assumption of O₃=0.35 [atm cm] (below) for grassland at VIS channel with R_{toa}=0.12 (left) and at NIR channel with R_{toa}=0.35 (right). SZA=VZA=45 degrees, AOD kept constant at 0.1.

The O₃ test results are as expected when compared to e.g. the comprehensive AVHRR atmospheric correction study by Tanré et al. (1992). Ozone has virtually no effect on the NIR channel, as there are no ozone absorption bands in those wavelengths, but it has an effect on the VIS channel. The relative error caused by the constant O₃ of 0.35 [atm cm] is no more than 5% in the typical range of O₃ content (given by Tanré et al. (1992) as 0.25-0.5 atm cm).

We again evaluate the effect on the broadband albedo by simulating SAL with a variation in O₃. Using O₃=0.35 with all other inputs as stated above gives a SZA-normalized broadband albedo of **0.277**. Changing the O₃ content to 0.5 changes the SZA-normalized broadband albedo to **0.282**, a relative difference of **~1.9%**. The O₃ assumption impact on broadband albedo is visualized in Figure 24.

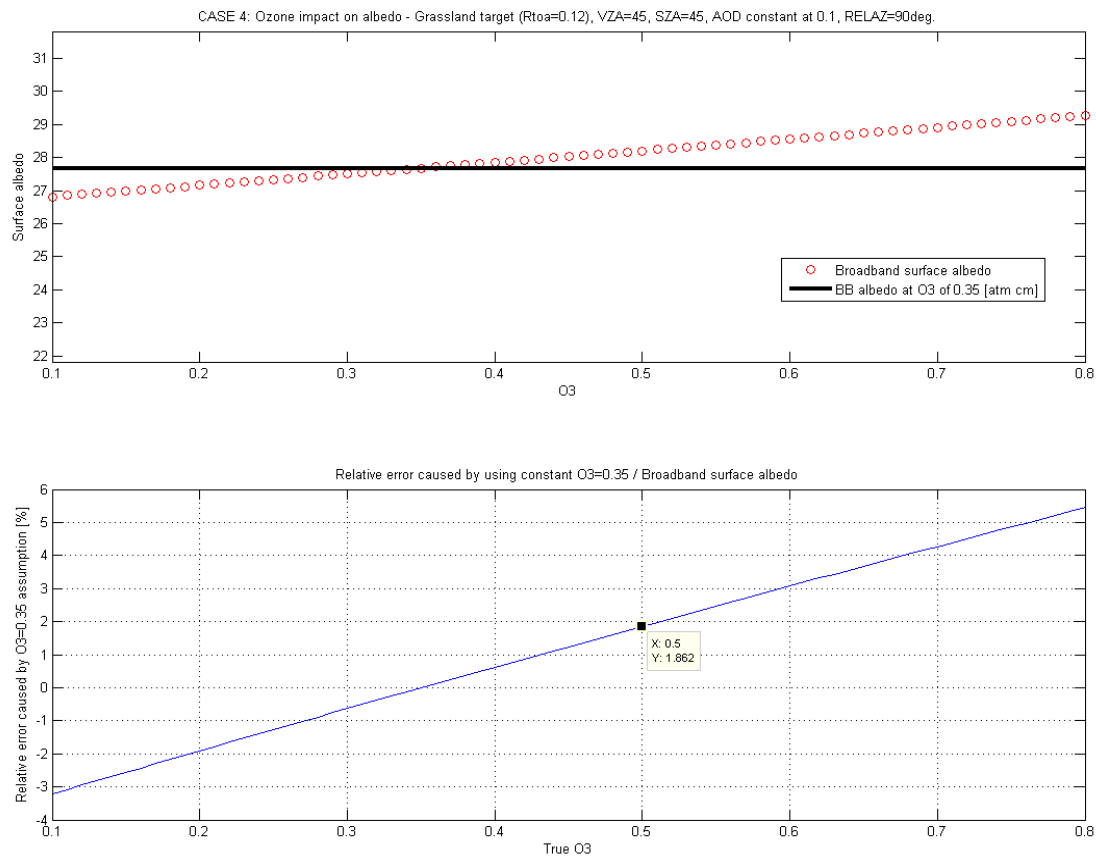


Figure 24: The impact of using a constant O3 on the resulting broadband albedo in Case 4. Above: the calculated broadband albedo using various O3 values in the atmospheric correction. Below: Relative error in the broadband albedo calculated using O3=0.35[atm cm] relative to using a ‘true’ AOD value.

The difference is so small because the NIR reflectance dominates the broadband albedo over vegetation – and the NIR reflectance is invariant as regards to O3 content in the atmosphere (Tanré et al., 1992). This can be verified by examining the contribution of the various VIS and NIR spectral albedo terms to the narrow-to-broadband equation by Liang (2000) that is used for CLARA-SAL.

Contribution of terms in Liang narrow-to-broadband conversion to resulting broadband albedo (grassland target from Case 1)

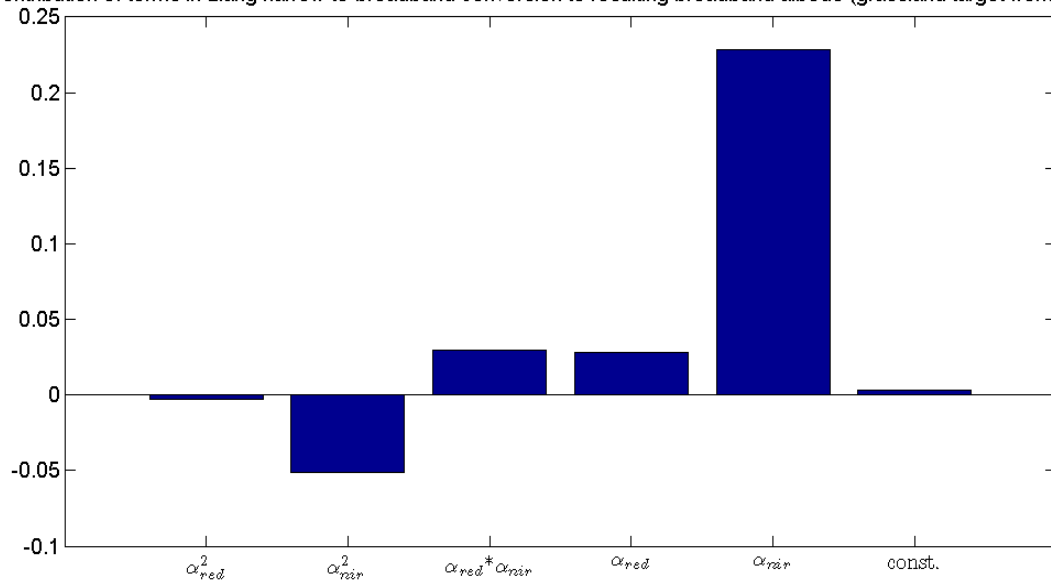




Figure 25: An example of the contribution of terms in Liang NTBC equation to the total broadband albedo. Inputs of Case 1 used (vegetated grassland, average viewing geometry).

Figure 25 shows the contribution of terms in Liang's NTBC equation to the total broadband black-sky surface albedo. The NIR albedo clearly dominates in the case of vegetation, so the error of applying constant ozone content is negligible. Over targets that are bright in the VIS channel like deserts and snow, the ozone content has more significance. Future efforts in CLARA-SAL development will include studies on including ozone content timeseries information from e.g. TOMS.

 	EUMETSAT SAF on CLIMATE MONITORING Algorithm Theoretical Basis Document Surface Albedo CLARA-A1	Doc.No.: SAF/CM/FMI/ATBD/GAC/SAL Issue: 1.2 Date: 11.06. 2012
---	--	---

Assumptions and Limitations

This chapter summarizes the main points concerning the assumptions and limitations of the algorithm. For details on the issues, the reader should see the previous section on error budget.

4.2.1 Assumptions and mandatory input

The main assumption of the CLARA-SAL algorithm is the correctness of the cloud mask input. Also, beside normal sanity checking, the input data is not monitored for large variations between overpasses or other signs of anomalous behaviour. On the other hand, because of the large change in surface albedo during snowfall, a change monitoring tool would be challenging to implement while considering the fact that some large and sudden variations in albedo are natural.

The algorithm also inherently assumes that the land use classification information is always accurate, and that the BRDF models work equally well in all geographical areas and during all seasons. This may not always be the case.

The mandatory inputs for the algorithm are



- Red and NIR channel TOA reflectances (AVHRR/SEVIRI ch. 1 & 2)
- Sun Zenith Angles
- Satellite Zenith angles
- Relative Azimuth angles between Sun and the satellite / Separate Sun and Satellite Azimuth angles required for reliable topography correction computation
- Cloud mask
- Cloud mask quality data
- Land cover data
- SMAC atmospheric correction coefficients

4.2.2 Constraints and Limitations

CLARA-SAL computation is dependent upon clear-sky conditions and appropriate Sun-satellite geometry. The existence of clouds precludes surface albedo retrieval and therefore such areas are masked out. As for the sun-satellite geometry, the atmospheric and BRDF corrections become unreliable when the either the Sun or the satellite are too low over the horizon. Therefore, CLARA-SAL computation is limited to times when Sun zenith angle < 70 degrees and satellite zenith angle < 60 degrees.

Ocean albedo is also currently fixed to a single constant. A realistic reproduction of ocean albedo would require the input of chlorophyll content, as well as wind speed data for wave effect consideration. The algorithm is equipped to handle such input, operational implementation is planned for CLARA-SAL Edition 2.

The accuracy of the cloud mask is critical to the SAL product quality. Cloud overestimation in the mask is not a problem since the weekly and monthly SAL end products generally have sufficient sampling to compensate. However, underestimation of clouds may lead to sporadic instantaneous surface albedo retrieval overestimations of several hundred per cent (relative). Over snow-covered areas, the underestimation of cloud cover typically leads to an underestimation of the instantaneous surface albedo. The end products are resistant to such effects because they are the result of averaging of instantaneous products, leading to mitigation of sporadic errors. The quantification of the robustness of SAL end products to



 	EUMETSAT SAF on CLIMATE MONITORING Algorithm Theoretical Basis Document Surface Albedo CLARA-A1	Doc.No.: SAF/CM/FMI/ATBD/GAC/SAL Issue: 1.2 Date: 11.06. 2012
---	--	---

cloud mask errors is yet to be performed.

The current atmospheric correction is a compromise between the need to avoid introducing artificial retrieval errors into product and a desire to correctly account for the atmospheric physics affecting the surface albedo retrieval. We currently use an atmospheric model to account for the second-order atmospheric variables that affect surface albedo retrievals, namely columnar water vapour and surface pressure. Ozone content of the atmosphere is kept constant. However, the most important atmospheric variable affecting the surface albedo retrievals is the aerosol optical depth (AOD) in the atmosphere. Variations in AOD are both regional and global; their effect in space-observed surface reflectances is substantial. Yet an accurate derivation of AOD from satellite observations to support surface albedo retrievals requires assumptions on the albedo of the underlying surface. Through making these assumptions, the product contains an internal correlation between the AOD and the albedo of the terrain underneath, which is an undesired combination. To avoid this, we currently choose to use a fixed AOD content in the atmosphere everywhere. Though additional albedo retrieval errors will occasionally occur as a result, we make this choice consciously in order to preserve the trend analysis capabilities of the CLARA-SAL product. This also gives the possibility to reverse engineering: as every pixel has a constant AOD, it is relatively simple to estimate, how much the albedo would change from the default atmosphere case, if on gets information of the true atmosphere in some regions.



One may also attempt to solve the aerosol-albedo problem by a simultaneous retrieval of both quantities. Such a method has been proposed and implemented for MSG/SEVIRI by Govaerts et al. (2010). While proven effective (Wagner et al., 2010), the technique requires a large amount of daily observations for each retrieval location and is computationally fairly expensive. Therefore we do not attempt to implement a similar procedure for CLARA-SAL. In addition, combining topography correction and simultaneous aerosol-albedo problem might not be realistic, as the topography correction is already such a heavy task, that neighbour pixel interaction can't be taken into account.

Errors in the land use classification data are another source of retrieval error that should be considered. The LUC data is not continuously updated, therefore man-made or natural changes in land cover are generally not correctly picked up by CLARA-SAL, which is dependent on LUC data to choose a proper surface albedo subroutine. A known location where errors do occur is the ablation zone in West Greenland for Arctic SAL. There broken terrain, ice flows and progressing snow melt in summer seasons cause the LUC classification to be inaccurate, leading to major retrieval errors. Also, the algorithm does not yet properly delineate between desert areas and other barren terrain, leading to increased retrieval errors for desert. Since the CLARA-SAL dataset covers 28 years in time, inaccuracies in the USGS classification are unavoidable. Their effect and source is also very difficult to localize in time or space.

 	EUMETSAT SAF on CLIMATE MONITORING Algorithm Theoretical Basis Document Surface Albedo CLARA-A1	Doc.No.: SAF/CM/FMI/ATBD/GAC/SAL Issue: 1.2 Date: 11.06. 2012
---	--	---

References

- Briegleb, B.P. , Minnis, P. , Ramanathan, V. and Harrison, E., 1986: Comparison of regional clear-sky albedos inferred from satellite observations and model computations. *Journal of Climate and Applied Meteorology*, **25**, 214–226.
- Derrien, M. and H. LeGléau, 2005: MSG/SEVIRI cloud mask and type from SAFNWC. *International Journal of Remote Sensing*, **26**, 4707–4732.
- DeAbreu, R.A. Jeffrey Key, J.A. Maslanik, M.C. Serreze, and E.F. LeDrew, 1994: Comparison of in situ and AVHRR-derived broadband albedo over arctic sea ice. *Arctic*, **47**(3), 288–297.
- Dickinson, R.E. Land surfaces processes and climate - surface albedos and energy balance, 1983: *Advances in Geophysics*, **25**, 305–353.
- Dybbroe, A., Thoss, A. and K-G. Karlsson, 2005: SAFNWC AVHRR cloud detection and analysis using dynamic thresholds and radiative transfer modelling part I: Algorithm description. *Journal of Applied Meteorology*, **44**, 39–54.
- European Environment Agency, 2004: Corine land cover 2000 - mapping a decade of change. *Brochure 4*, European Environment Agency.
- GCOS Secretariat, 2006: Systematic observation requirements for satellite-based products for climate. *Technical Report 107*, Global Climate Observing System, World Meteorological Organization, 7 bis, Avenue de la Paix P.O. Box No. 2300 CH-1211 Geneva 2, Switzerland.
- Govaerts, Y. M., Wagner, S., Lattanzio, A., and Watts, P., 2010: Joint retrieval of surface reflectance and aerosol optical depth from MSG/SEVIRI observations with an optimal estimation approach: 1. Theory, *J. Geophys. Res.*, **115**, D02203, doi:10.1029/2009JD011779
- Heidinger, A.K., Straka III, W.C., Molling, C.C., Sullivan, J.T. & Wu, X., 2010: Deriving an inter-sensor consistent calibration for the AVHRR solar reflectance data record, *International Journal of Remote Sensing*, **31**:24, 6493-6517
- Jin, Z., Charlock, T.P. Smith, Jr, William L. and Rutledge, K, 2004: A parameterization of ocean surface albedo. *Geophysical Research Letters*, **31**, L22301.
- Jin, Z., Charlock, T.P., Rutledge, K., Stamnes, K., and Wang, Y., 2006: Analytical solution of radiative transfer in the coupled atmosphere-ocean system with a rough surface. *Appl. Opt.*, **45**, 7443-7455.
- Karlsson, K.-G. and Dybbroe, A. 2010: Evaluation of Arctic cloud products from the EUMETSAT Climate Monitoring Satellite Application Facility based on CALIPSO-CALIOP observations. *Atmospheric Chemistry and Physics*, **10**, 1789-1807.
- Kaufman Y.J., Tanré, D., 1996: Strategy for direct and indirect methods for correcting the aerosol effect on remote sensing: From AVHRR to EOS-MODIS, *Remote Sensing of Environment*, **55**(1), pp. 65–79, 1996.

 	EUMETSAT SAF on CLIMATE MONITORING Algorithm Theoretical Basis Document Surface Albedo CLARA-A1	Doc.No.: SAF/CM/FMI/ATBD/GAC/SAL Issue: 1.2 Date: 11.06. 2012
---	--	---

Li, Z. Cihlar, J., Zheng, X., Moreau, L., and Ly, H, 1996: The bidirectional effects of AVHRR measurements over boreal regions. *IEEE Transactions on Geoscience and Remote Sensing*, **34**(6), 1308–1322.

Liang, S. Strahler, A.H. and Walthall, C, 1999: Retrieval of land surface albedo from satellite observations: A simulation study. *Journal of Applied Meteorology*, **38**, 712–725.

Liang, S, 2000: Narrowband to broadband conversions of land surface albedo I: Algorithms. *Remote Sensing of Environment*, **76**, 213–238.

Manninen, T. Andersson, K. Breivik, L-A. and Gratzki, A., 2005: Surface albedo of arctic sea ice operationally - co-operation of CM SAF and ocean and sea ice SAF. In *Proceedings of the 2005 EUMETSAT Meteorological Satellite Conference*.

Manninen, T., 2003: Scientific prototype report - validation of surface albedo product. *Technical report*, FMI (for the CM SAF project).

Manalo-Smith, N., Smith, G.L., Tiwari, S.N. and Staylor, W.F, 1998: Analytic forms of bidirectional reflectance functions for application to earth radiation budget studies. *Journal of Geophysical Research*, **103**(D16), 19733–19752.

Nicodemus, F.E., 1970: Reflectance nomenclature and directional reflectance and emissivity. *Applied Optics*, **9**(6), 1474–1475.

Proud, S.R., Rasmussen, M.O., Fensholt, R., Sandholt, I., Shisanya, C., Wycliffe, M., Mbow, C. and Anyamba, A, 2010: Improving the SMAC atmospheric correction code by analysis of Meteosat Second Generation NDVI and surface reflectance data. *Remote Sensing of Environment*, **114**(8), 1687-1698.



Rahman, H. and Dedieu, G., 1994: SMAC: a simplified method for the atmospheric correction of satellite measurements in the solar spectrum. *International Journal of Remote Sensing*, **15**, 123-143.

Riihelä A., Laine V., Manninen T., Palo T., Vihma T., 2010: Validation of the CM SAF surface broadband albedo product: Comparisons with in situ observations over Greenland and the ice-covered Arctic Ocean. *Remote Sensing of Environment*, **114** (11), 2779-2790.

Roujean, J.L., Leroy, M., and Deschamps, P-Y., 1992: A bidirectional reflectance model of the earth's surface for the correction of remote sensing data. *Journal of Geophysical Research*, **97**(18), 20455–20468.

Schaepman-Strub, G., Schaepman, M.E., Painter, T.H., Dangel, S., Martonchik, J.V., 2006: Reflectance quantities in optical remote sensing – definitions and case studies. *Remote Sensing of Environment*, **103**, 27-42.

Song, J. and Gao, W., 1999: An improved method to derive surface albedo from narrowband AVHRR satellite data: narrowband to broadband conversion. *Journal of Applied Meteorology*, **38**, 239–249.

 	<p align="center">EUMETSAT SAF on CLIMATE MONITORING</p> <p align="center">Algorithm Theoretical Basis Document Surface Albedo CLARA-A1</p>	<p>Doc.No.: SAF/CM/FMI/ATBD/GAC/SAL</p> <p>Issue: 1.2</p> <p>Date: 11.06. 2012</p>
---	--	--

Tanré, D.; Holben, B.N.; Kaufman, Y.J., 1992; Atmospheric correction against algorithm for NOAA-AVHRR products: theory and application, *IEEE TGRS* **30**(2), pp.231 - 248

van Leeuwen, W.J.D. and Roujean, J.L., 2002: Land surface albedo from the synergistic use of polar (EPS) and geo-stationary (MSG) observing systems: An assessment of physical uncertainties. *Remote Sensing of Environment*, **81**, 273–289.


Vermote, E., Tanré, D., Deuzé, J., Herman, M., and Morcrette, J.J., 1997: Second Simulation of the Satellite Signal in the Solar Spectrum, 6S: An Overview. *IEEE TGRS*, **35**(3), 675-686.

Wagner, S. C., Govaerts, Y.M., and Lattanzio, A., 2010: Joint retrieval of surface reflectance and aerosol optical depth from MSG/SEVIRI observations with an optimal estimation approach: 2. Implementation and evaluation, *J. Geophys. Res.*, **115**, D02204, doi:10.1029/2009JD011780.

Wang, X. and Zender, C.S., 2011: Arctic and Antarctic Diurnal and Seasonal Variations of Snow Albedo from Multi-year BSRN Measurements. *Journal of Geophysical Research*, **116**, F03008, 16 PP., doi:10.1029/2010JF001864

Wu, A. Li, Z. and Cihlar, J., 1995: Effects of land cover type and greenness on advanced very high resolution radiometer bidirectional reflectances: Analysis and removal. *Journal of Geophysical Research*, **100**(D5), 9179–9192.

Xiong, X., Stamnes, K. and Lubin D., 2002: Surface albedo over the arctic ocean derived from AVHRR and its validation with SHEBA data. *Journal of Applied Meteorology*, **41**, 413–425.

	EUMETSAT SAF on CLIMATE MONITORING Algorithm Theoretical Basis Document Surface Albedo CLARA-A1	Doc.No.: SAF/CM/FMI/ATBD/GAC/SAL Issue: 1.2 Date: 11.06. 2012
---	--	---


Appendix A. Symbols and Abbreviations

Mathematical Symbols



Symbol	Meaning	Unit
α	Albedo	unitless
θ	Zenith angle	°
φ	Azimuthal angle	°
λ	Wavelength	m
ρ	Reflectance from a direction to a direction	sr^{-1}
Ω	Anisotropy factor (reflectance relative to nadir)	sr^{-1}
γ	Scattering angle	°
Γ	Fraction of the difference and sum of red and NIR reflectance	unitless
E	Irradiance	W / m^2
f	Frequency	Hz
F	Radiant Flux	W
L	Radiance	$W \cdot sr^{-1} \cdot m^{-2}$
R	Reflectivity	unitless

Abbreviations

AOD	Aerosol Optical Depth
AVHRR	Advanced Very High Resolution Radiometer (NOAA)
BB	Broadband
BRDF	Bidirectional Reflectance Distribution Function
BSRN	Baseline Surface Radiation Network
CM SAF	Satellite Application Facility on Climate Monitoring
DEM	Digital Elevation Model
DWD	Deutscher Wetterdienst
ECMWF	European Center for Medium-Range Weather Forecasts
ECV	Essential Climate Variable
EUMETSAT	European Organisation for the Exploitation of Meteorological Satellites
EPS	Enhanced Polar System
FMI	Finnish Meteorological Institute
GOS	Global Climate Observing System
IPCC	Intergovernmental Panel on Climate Change
KNMI	Koninklijk Nederlands Meteorologisch Instituut (Royal Netherlands Meteorological Institute)
LUC	Land Use Classification
LUT	Look-Up Table
MODIS	Moderate Resolution Imaging Spectroradiometer
NOAA	National Oceanic and Atmospheric Administration
NTB (C)	Narrow-to-Broadband (Conversion)
NWC-SAF	Nowcasting Satellite Application Facility
NWP	Numerical Weather Prediction
OSI-SAF	Ocean and Sea Ice Satellite Application Facility
PNG	Portable Network Graphics
PPS	Polar Platform System
RMIB	Royal Meteorological Institute of Belgium

	<p align="center">EUMETSAT SAF on CLIMATE MONITORING</p> <p align="center">Algorithm Theoretical Basis Document Surface Albedo CLARA-A1</p>	<p>Doc.No.: SAF/CM/FMI/ATBD/GAC/SAL</p> <p>Issue: 1.2</p> <p>Date: 11.06. 2012</p>
---	---	--

SAF	Satellite Application Facility
CLARA-SAL	Global Area Coverage Surface ALbedo product
SEVIRI	Spinning Enhanced Visible and Infra-Red Imager
SMAC	Simplified method for the atmospheric correction of satellite measurements in the solar spectrum
SMHI	Swedish Meteorological and Hydrological Institute
SZA	Sun Zenith Angle
TOA	Top of Atmosphere
TOMS	Total Ozone Mapping Spectrometer
UNFCCC	United Nations Framework Convention on Climate Change
USGS	United States Geological Survey
VZA	Viewing Zenith Angle

 	EUMETSAT SAF on CLIMATE MONITORING Algorithm Theoretical Basis Document Surface Albedo CLARA-A1	Doc.No.: SAF/CM/FMI/ATBD/GAC/SAL Issue: 1.2 Date: 11.06. 2012
---	--	---

Appendix B: SMAC numeric equations for correction terms X, Y, Z:

$$\begin{aligned} Z &= d - (\omega_0) * 3 * (g) * \mu_v * dp + (\omega_0) * aer_phase / 4 ; \\ X &= c1 - (\omega_0) * 3 * (g) * \mu_v * cp1 ; \\ Y &= c2 - (\omega_0) * 3 * (g) * \mu_v * cp2 ; \end{aligned}$$

where

$$\begin{aligned} aer_phase &= (a0P) + (a1P) * \xi + (a2P) * \xi * \xi + (a3P) * power(\xi, 3) + \\ &(a4P) * power(\xi, 4); \\ ak2 &= (1 - (\omega_0)) * (3 - (\omega_0) * 3 * (g)) ; \\ ak &= sqrt(ak2) ; \\ e &= -3 * \mu_s * \mu_s * (\omega_0) / (4 * (1 - ak2 * \mu_s * \mu_s)) ; \\ f &= -(1 - (\omega_0)) * 3 * (g) * \mu_s * \mu_s * (\omega_0) / (4 * (1 - ak2 * \mu_s * \mu_s)) ; \\ dp &= e / (3 * \mu_s) + \mu_s * f ; \\ d &= e + f ; \\ b &= 2 * ak / (3 - (\omega_0) * 3 * (g)) ; \\ del &= exp(ak * \tau_p) * (1 + b) * (1 + b) - exp(-ak * \tau_p) * (1 - b) * (1 - b) ; \\ ww &= (\omega_0) / 4 ; \\ ss &= \mu_s / (1 - ak2 * \mu_s * \mu_s) ; \\ q1 &= 2 + 3 * \mu_s + (1 - (\omega_0)) * 3 * (g) * \mu_s * (1 + 2 * \mu_s) ; \\ q2 &= 2 - 3 * \mu_s - (1 - (\omega_0)) * 3 * (g) * \mu_s * (1 - 2 * \mu_s) ; \\ q3 &= q2 * exp(-\tau_p / \mu_s) ; \\ c1 &= ((ww * ss) / del) * (q1 * exp(ak * \tau_p) * (1 + b) + q3 * (1 - b)) ; \\ c2 &= -((ww * ss) / del) * (q1 * exp(-ak * \tau_p) * (1 - b) + q3 * (1 + b)) ; \\ cp1 &= c1 * ak / (3 - (\omega_0) * 3 * (g)) ; \\ cp2 &= -c2 * ak / (3 - (\omega_0) * 3 * (g)) ; \end{aligned}$$

in the preceding code, a0P, a1P, a2P, a3P and a4P are predefined constants from the SMAC coefficient file.